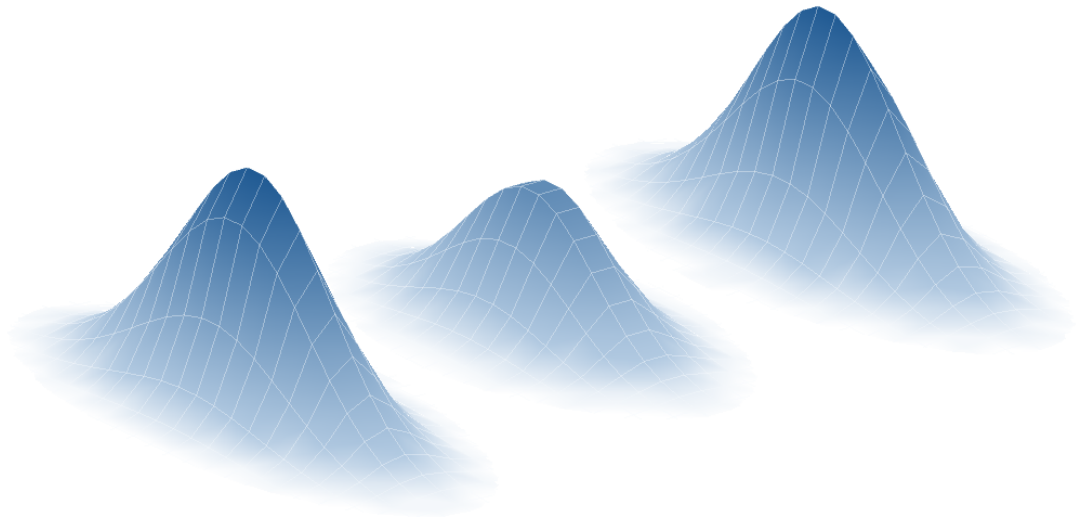


# Theoretical investigations of dipolar quantum gases in multi-well potentials

Diplomarbeit  
vorgelegt von

**David Peter**



Hauptberichter: Prof. Dr. Tilman Pfau  
Mitberichter: Prof. Dr. Hans Peter Büchler

5. Physikalisches Institut  
Universität Stuttgart

16. September 2011



**Erklärung:**

Hiermit erkläre ich, dass ich diese Arbeit selbständig verfasst und keine anderen als die angegebenen Quellen und Hilfsmittel benutzt habe.

Stuttgart, den 16. September 2011

---

(David Peter)



# Contents

<b>Introduction</b>	<b>7</b>
<b>1. Dipolar quantum gases</b>	<b>9</b>
1.1. Bose-Einstein condensation . . . . .	9
1.2. Interactions . . . . .	10
1.2.1. Contact interaction . . . . .	10
1.2.2. Dipolar interaction . . . . .	11
1.3. Mean-field description . . . . .	13
1.3.1. Gross-Pitaevskii equation . . . . .	13
1.3.2. Mean-field description including dipolar interactions . . . . .	15
1.3.3. Dimensionless form of the Gross-Pitaevskii equation . . . . .	16
1.3.4. Approximate solutions in a harmonic trap . . . . .	18
1.4. Basic properties . . . . .	19
1.4.1. Stability of dipolar quantum gases . . . . .	19
1.4.2. Fourier transform of the dipolar potential . . . . .	20
<b>2. Multi-well physics</b>	<b>23</b>
2.1. Multi-well potentials . . . . .	23
2.2. Inter-site energy . . . . .	24
2.2.1. Limiting cases . . . . .	27
2.2.2. On-site energy as a special case . . . . .	28
2.3. Energy functional for Gaussian wave functions . . . . .	29
<b>3. Bose-Hubbard model</b>	<b>31</b>
3.1. Derivation . . . . .	31
3.2. Double-well system . . . . .	33
3.3. Triple-well system . . . . .	34
3.4. More wells: complexity of the problem . . . . .	34
<b>4. Variational method</b>	<b>37</b>
4.1. Derivation and approximations . . . . .	37
4.2. Recursive algorithm to find the ground state . . . . .	38
4.3. Exact solution for few wells . . . . .	40
4.3.1. Solution for two wells . . . . .	40
4.3.2. Solution for three wells . . . . .	40

4.4. General features of the multi-well states . . . . .	42
4.4.1. Dependence on the cut-off parameter . . . . .	44
<b>5. Scaling of the interaction energy</b>	<b>45</b>
5.1. On-site interaction energy . . . . .	45
5.2. Gaussian trial function . . . . .	46
5.2.1. Dimensional crossover . . . . .	47
5.3. Thomas-Fermi regime . . . . .	47
5.4. Comparison to the numerical solution . . . . .	49
<b>6. Numerical simulations</b>	<b>51</b>
6.1. Methods . . . . .	51
6.1.1. Imaginary time evolution . . . . .	51
6.1.2. Split-step method . . . . .	52
6.2. Preparations . . . . .	54
6.2.1. Verification of the results . . . . .	54
6.2.2. Procedure for a multi-well simulation . . . . .	54
6.3. Triple-well simulations . . . . .	56
6.3.1. Geometrical considerations . . . . .	56
6.3.2. Interaction parameters . . . . .	57
6.3.3. Repulsive inter-site energy . . . . .	58
6.3.4. Attractive inter-site energy . . . . .	60
6.3.5. Combined picture . . . . .	60
<b>Conclusions and outlook</b>	<b>63</b>
<b>A. Experimental parameters</b>	<b>65</b>
A.1. Dipolar gases . . . . .	65
A.2. Interaction parameters . . . . .	66
A.3. The single wells . . . . .	67
<b>B. Supplementary calculations</b>	<b>69</b>
B.1. Changed aspect ratio . . . . .	69
B.2. Changed depth of the potential . . . . .	69
<b>C. Documentation of the simulation program</b>	<b>71</b>
C.1. Concept and structure . . . . .	71
C.2. Setting up the program . . . . .	72
C.3. Scripting interface . . . . .	73
<b>Bibliography</b>	<b>77</b>
<b>Danksagung</b>	<b>81</b>

# Introduction

## Motivation

Since the experimental achievement of the first Bose-Einstein condensates in 1995 [1–3], the focus has shifted from basic properties of the ultracold gases to applications where the quantum degenerate samples are used as a tool to model various kinds of physical systems.

Describing strongly interacting electrons in solids, for example, is a complex many-body problem due to thermal defects and impurities in the crystalline structure. In contrast, quantum gases provide clean model systems due to the ultralow temperatures and the isolation from the environment. Both the preparation of the system and the measurement of its properties profit from the macroscopic size of the quantum objects. External and internal degrees of freedom can be read out and controlled in almost any desired way.

An important aspect of ultracold gases concerns the inter-particle interactions which can be precisely adjusted [4]. As the first Bose-Einstein condensates were consisting of the alkali atoms rubidium, lithium and sodium, only the short-ranged and isotropic contact interactions were significant.

With the condensation of highly dipolar atomic species like  $^{52}\text{Cr}$  in 2005 [5], long-ranging and anisotropic interactions became relevant, allowing to investigate new regimes of interacting many-body systems [6]. Since then, several experimental and theoretical studies have been done on dipolar quantum gases. The stability and the collapse dynamics of dipolar condensates have been investigated in detail [7–9]. A roton-maxon spectrum inducing structured ground states has been predicted [10, 11].

Another constituent of modern experiments are optical potentials which offer widely tunable energy landscapes. Among them, optical lattices have been extensively studied and quantum phase transitions from a superfluid to a Mott insulator have been observed [12]. New quantum phases of dipolar quantum gases in optical lattices, like checkerboard or supersolid phases, have also been predicted [13].

In this work we will focus on multi-well potentials. Compared to the optical lattices where usually an infinite number of sites is assumed, the attention is turned on a fixed number of wells and the detailed behavior of the quantum gas when loaded into such a potential. The multi-well system can act as a minimal model system for larger periodic structures but it also leads to new aspects due to its finite size. Interesting ground states and phases have been predicted for a dipolar triple-well system [14]. The key idea is to use mesoscopic samples of dipolar particles to enhance the overall dipolar effect. Due to the long-ranging interaction a new aspect enriches the system compared to non-dipolar gases:

neighboring wells are able to interact without exchange of particles. Even wells which are further apart influence each other, although in a significantly weaker way. Depending on the sign and strength of this inter-site interaction, different states can be observed. The long-range character is clearly revealed in states such as the one shown on the title page where the dipolar repulsion leads to a flow of particles to the outer wells.

### About this thesis

This thesis is mainly of theoretical nature. Nevertheless, there has been a close collaboration with the experimentalists in our group. Especially the numerical simulations have been largely influenced by discussions about the upcoming experiment which will have all the tools ready to investigate dipolar quantum gases in multi-well potentials [15]. Some investigations were directly motivated by experimental conditions (chapters 5 and 6). Still this work is not meant to be restricted by experimental limitations and is in large parts also applicable to similar systems with different dipolar species or other trapping potentials.

The thesis is organized as follows: chapter 1 gives an introduction to the physics of ultracold dipolar quantum gases and provides all necessary information for the applications in the subsequent parts of the work. We introduce important topics of the multi-well physics in chapter 2 and come to the first application in chapter 3 which shows how to apply the Bose-Hubbard model to the situation of a multi-well potential. We will start with the double-well system and show that it is not suited as a minimal model system as it provides no new features compared to the non-dipolar case. Instead we will henceforth use the triple-well as our toy system to show important aspects of the multi-well physics. As the direct solution of the Bose-Hubbard model is computationally out of reach for more than three wells, we will introduce the variational method in chapter 4. With this method, although approximate, we are able to find ground states for much larger numbers of wells. Both methods, the direct solution of the Bose-Hubbard model and the variational method, are only valid if the number of particles in each well is small. We will demonstrate this in chapter 5 and show how the interaction energy scales with the particle number. As this scaling cannot be included in our previous models, we take a third approach in the final chapter 6: we solve numerically the dipolar Gross-Pitaevskii equation in the multi-well potential. This allows us to investigate the system in the regime of large particle numbers. We compare our results to the previous methods and show that new aspects, like the stability of the dipolar condensate, have to be taken into account.

The appendix provides some information about the comparison to the experimental parameters, supplementary calculations done with the simulation program and a detailed technical documentation of the simulation program.



# 1. Dipolar quantum gases

*This introductory chapter will explain the basic physics of dipolar quantum gases. We will first introduce the notion of a quantum gas and describe the behavior of ultracold bosonic particles.*

*Inter-particle interactions will turn out to be a crucial ingredient at low temperatures and we will deal with two basic types of interactions: the contact-interaction whose origin is hidden in the detailed atomic properties of the gas particles and the dipolar interaction with its characteristic features.*

*Treating each individual degree of freedom in a gas is an impossible intent. For a large number of particles though we can describe the whole ensemble in a mean field approach. The task is thereby reduced to a single particle problem. The single particle, in this picture, is interacting with a field which is generated by all the other particles.*

## 1.1. Bose-Einstein condensation

To study quantum effects in a thermal gas one necessarily has to deal with low temperatures and high densities. The quantum nature of the particles becomes important if their inherent wavelength is comparable or larger than the distance to the surrounding atoms or molecules. The important quantities are therefore the thermal de-Broglie wavelength  $\lambda_{\text{therm}}$  and the mean inter-particle distance  $n^{-1/3}$  with the gas density  $n$ .

Depending on the statistics—and therefore on the spin—of the particles the system undergoes a phase transition if the ratio of the two indicated quantities exceeds a certain value. Throughout this thesis we will concentrate on bosonic particles.

An ideal Bose gas undergoes a phase transition if the following condition is fulfilled (where  $\zeta$  is the Riemann zeta function) [16–18]:

$$\frac{\lambda_{\text{therm}}}{n^{-1/3}} = \zeta(3/2)^{2/3} \approx 1.9.$$

The emerging phase of the Bose gas is called Bose-Einstein condensate (BEC). We will focus on the condensed state and indeed neglect *all* temperature effects in the following. This  $T = 0$  approximation leads to certain simplifications in the description of the quantum gas.

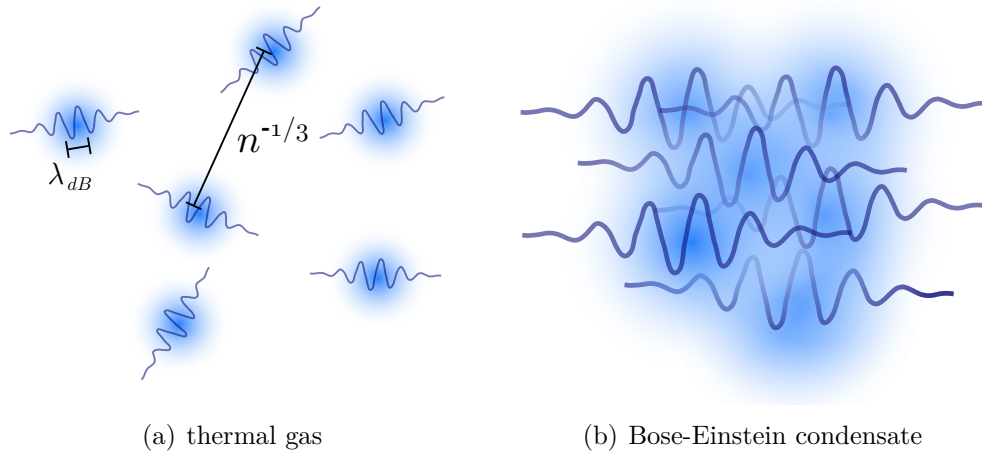


**Figure 1.1.:** Naive visualization of the phase transition from a (normal) thermal gas to a quantum degenerate state, the Bose-Einstein condensate. The important length scales are the de Broglie wavelength and the inter-particle distance. In the thermal gas the wavelength of the particles is too small to support coherent effects. In the Bose-Einstein condensate the different waves are overlapping and the whole system turns into a macroscopic matter wave.

## 1.2. Interactions

An important aspect of ultracold gases are the interactions between the particles. Compared to a thermal gas the inter-particle interactions in cold samples can easily be as strong as (or much larger than) the thermal effects.

We will see that we have to distinguish between two different kind of interactions depending on the extension of the potential.

### 1.2.1. Contact interaction

Applying the formalism of scattering theory in the low temperature limit shows that for bosons only the s-wave scattering remains, due to the energy barriers for higher orbital momentum [19, chapter 3.1.2].

The real particle-particle interaction potential can be mapped to a hard-sphere potential as long as it is of finite size or falls off like  $r^{-n}$  with  $n > 3$  for  $r \rightarrow \infty$  [19, chapter 3.1.3]. This is possible for most molecular potentials. The van-der-Waals potential for example is proportional to  $r^{-6}$  in the limit of large distances.

The s-wave scattering can be included in the description by an effective interaction

which has a delta-function potential<sup>1</sup>:

$$V = g \delta(\mathbf{r}_1 - \mathbf{r}_2). \quad (1.1)$$

The coupling constant  $g$  which determines the interaction strength is connected with the s-wave scattering length  $a$  by

$$g \equiv \frac{4\pi\hbar^2}{m}a, \quad (1.2)$$

where  $m$  is the mass of one particle.

Using the pseudo potential (1.1) is only a reasonable approximation if the gas is dilute. This diluteness condition can be stated as  $na^3 \ll 1$ . Note that this does not imply that the interactions have to be small. Compared to the kinetic energy of the gas, the interaction energy can still be much larger and the behavior of the gas can therefore be *non-ideal* [17, chapter 3].

The important features of this contact interaction are the spatial isotropy and the short range of the potential.

### 1.2.2. Dipolar interaction

Apart from the contact interaction there can be long-range interactions in quantum gases. We will call an inter-particle potential *long-range* if it falls off like  $r^{-n}$  with  $n \leq 3$  and *short-range* for  $n > 3$ . The reason for the division into short-range and long-range potentials is that only the short-range potentials can be included into the scattering length  $a$ , as mentioned in the last chapter<sup>2</sup>.

Out of the four fundamental forces only electromagnetic interactions can be sufficiently strong to have an effect on the overall behavior of the quantum gas. Therefore we can consider the multipole expansion to find possible long-range interactions.

The strongest interaction—from the viewpoint of the power law—would be monopole interactions (Coulomb- or gravity-like). Although there are proposals to realize an induced monopolar interaction [21] we will not consider them here. To our knowledge, an experimental realization has not been achieved, yet. The next term in the expansion is the dipole term which is just at the “edge” of the long-range part with a  $r^{-3}$  power-law.

Different atomic or molecular properties can give rise to dipolar interactions. These can either be of electric or magnetic origin. We will not go into the atomic details here, as the dipolar physics is universal and independent from the nature of the force. In both

---

<sup>1</sup>The real potential which yields the same scattering length, introduced initially by Fermi, is given by  $g\delta(\mathbf{r}_1 - \mathbf{r}_2) \frac{\partial}{\partial r_{12}} r_{12} \Big|_{r_{12}=0}$ . We ignore the regularizing operator as it has no effect on wave functions which are regular for  $\mathbf{r}_1 = \mathbf{r}_2$ . For details see [19, chapter 3.2].

<sup>2</sup>In  $d$  dimensions the criterion should be replaced by the following [20]. If the interaction falls off like  $r^{-n}$  with  $n > d$ , the interaction is considered to be short-range. This means that dipolar interactions in  $d < 3$  dimensions are *short-range*.

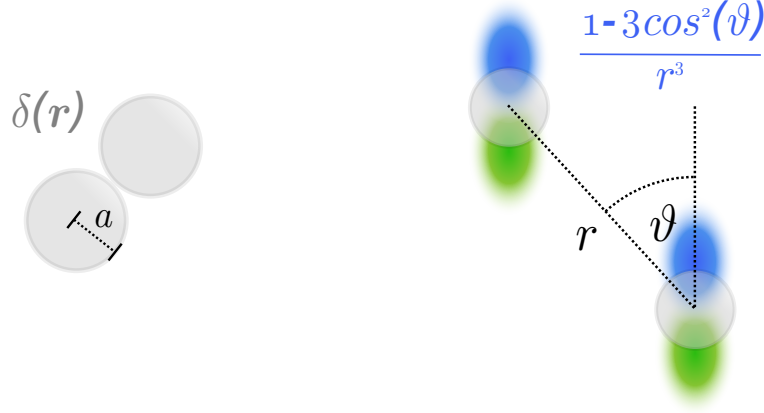


**Figure 1.2.:** Illustration of the two different interaction types in a dipolar quantum gas: the contact interaction (left) defined by the scattering length  $a$  is short-range and isotropic. The dipolar interaction (right) is long-range ( $\propto r^{-3}$ ) and anisotropic (angular dependence).

cases the interaction energy of two dipolar particles at positions  $\mathbf{r}_1$  and  $\mathbf{r}_2$  can be written as [22, chapter 4]

$$V_{\text{dd}}(\mathbf{r}_1, \mathbf{r}_2) = C_{\text{dd}} \times \frac{\boldsymbol{\mu}_1 \boldsymbol{\mu}_2 r^2 - 3(\boldsymbol{\mu}_1 \mathbf{r})(\boldsymbol{\mu}_2 \mathbf{r})}{r^5}$$

with the dipole moments  $\boldsymbol{\mu}_i$  and the inter-particle distance  $r = |\mathbf{r}| = |\mathbf{r}_1 - \mathbf{r}_2|$ .  $C_{\text{dd}}$  is a constant depending on the nature of the dipole forces<sup>3</sup>. Throughout this discussion we will deal with polarized dipoles. By applying a strong external field (electric or magnetic, depending on the dipole nature), all the dipoles in the gas can be aligned in the same direction. As we will only consider gases with one species of particles both the orientation and length of the dipole moments are the same  $\boldsymbol{\mu}_1 = \boldsymbol{\mu}_2 \equiv \boldsymbol{\mu}$ . The interaction energy simplifies to

$$V_{\text{dd}}(\mathbf{r}_1, \mathbf{r}_2) = C_{\text{dd}} \mu^2 \times \frac{1 - 3(\hat{\boldsymbol{\mu}} \hat{\mathbf{r}})^2}{r^3}$$

with the normalized vectors  $\hat{\mathbf{r}} = \mathbf{r}/|\mathbf{r}|$  and  $\hat{\boldsymbol{\mu}} = \boldsymbol{\mu}/|\boldsymbol{\mu}|$ . Defining the angle between the dipole moment  $\boldsymbol{\mu}$  and the displacement vector  $\mathbf{r}$  as  $\vartheta = \angle(\boldsymbol{\mu}, \mathbf{r})$  we end up at

$$V_{\text{dd}}(\mathbf{r}_1, \mathbf{r}_2) = \frac{C_{\text{dd}} \mu^2}{r^3} (1 - 3 \cos^2(\vartheta)).$$

---

<sup>3</sup>For magnetic dipoles  $C_{\text{dd}} = \frac{\mu_0}{4\pi}$ , for electric dipoles  $C_{\text{dd}} = \frac{1}{4\pi\epsilon_0}$

By the following definition the prefactor is written in a way which will be convenient:

$$g_{\text{dd}} \equiv \frac{4\pi C_{\text{dd}}\mu^2}{3}.$$

The parameter  $g_{\text{dd}}$  defines an effective coupling strength<sup>4</sup>. We finally obtain the dipole-dipole interaction potential

$$V_{\text{dd}}(\mathbf{r}_1, \mathbf{r}_2) = \frac{3}{4\pi} \frac{g_{\text{dd}}}{r^3} (1 - 3\cos^2(\vartheta)). \quad (1.3)$$

The characteristic features of the dipolar interaction are the long-range character due to the power law and the anisotropy caused by the angular dependence. There are two basic arrangements for interacting dipoles which are polarized. If they are placed head-to-tail ( $\rightarrow\rightarrow$ ) the interaction is attractive and twice as strong as the repulsive side-by-side configuration ( $\uparrow\uparrow$ ) at the same distance:

$$\begin{aligned} 1 - 3\cos^2(0) &= -2 \\ 1 - 3\cos^2(\pi/2) &= 1. \end{aligned}$$

### 1.3. Mean-field description

We want to describe the behavior of a dipolar quantum gas which consists of many interacting particles. As stated in the introduction, it is impossible to describe all degrees of freedom independently. One way around is to treat the interactions in a mean-field picture. We will briefly describe the necessary steps in the following section.

#### 1.3.1. Gross-Pitaevskii equation

To describe the dynamics of a system with interacting particles, one has to start with the general<sup>5</sup> many-body Hamiltonian [16–18]

$$\begin{aligned} \hat{H} = & \int d^3r \, \hat{\Psi}^\dagger(\mathbf{r}) \left[ -\frac{\hbar^2}{2m} \nabla^2 + V(\mathbf{r}) \right] \hat{\Psi}(\mathbf{r}) \\ & + \frac{1}{2} \int d^3r \int d^3r' \, \hat{\Psi}^\dagger(\mathbf{r}) \hat{\Psi}^\dagger(\mathbf{r}') V_{\text{int}}(\mathbf{r}, \mathbf{r}') \hat{\Psi}(\mathbf{r}') \hat{\Psi}(\mathbf{r}), \end{aligned} \quad (1.4)$$

where  $\hat{\Psi}^\dagger(\mathbf{r})$  and  $\hat{\Psi}(\mathbf{r})$  are the bosonic field operators creating and annihilating a particle at position  $\mathbf{r}$ , respectively.  $V(\mathbf{r})$  describes the external potential<sup>6</sup> and  $V_{\text{int}}(\mathbf{r}, \mathbf{r}')$  is the full two body interaction potential.

---

<sup>4</sup>We will also use the “dipolar length”  $a_{\text{dd}}$  defined by  $g_{\text{dd}} = \frac{4\pi\hbar^2 a_{\text{dd}}}{m}$ , analogous to the relation between  $g$  and the scattering length  $a$

<sup>5</sup>We neglect three-body interactions and higher-order terms.

<sup>6</sup>The external potential in our case will be the particle-trapping multi-well potential.

The field operators fulfill the usual bosonic commutation relations

$$[\hat{\Psi}(\mathbf{r}), \hat{\Psi}^\dagger(\mathbf{r}')] = \delta(\mathbf{r} - \mathbf{r}'), \quad [\hat{\Psi}(\mathbf{r}), \hat{\Psi}(\mathbf{r}')] = 0.$$

In general, the field operator

$$\hat{\Psi}(\mathbf{r}) = \sum_k \phi_k(\mathbf{r}) \hat{a}_k$$

can be expanded in terms of annihilation operators  $\hat{a}_k$  of a set of single particle states  $\phi_k$  with the relations

$$[\hat{a}_k, \hat{a}_l^\dagger] = \delta_{kl}, \quad [\hat{a}_k, \hat{a}_l] = 0.$$

Bose-Einstein condensation means that there is a macroscopic occupation of a single state (denoted by  $\psi_0$  in the following). In a mean-field description the operator character of  $\hat{a}_0$  and  $\hat{a}_0^\dagger$  is neglected. If the number of atoms  $N$  in the ground state is much larger than one, this approximation is legitimate because the operators are of the order of  $\sqrt{N}$  but the commutator is of the order of one<sup>7</sup>. We can therefore replace both operators by  $\sqrt{N}$ :

$$\begin{aligned} \hat{a}_0 &\approx \sqrt{N}, \\ \hat{a}_0^\dagger &\approx \sqrt{N}. \end{aligned}$$

Now we separate the ground state of the system  $\phi_0 \equiv \Psi$  from the rest, leading to

$$\hat{\Psi} = \sqrt{N} \cdot \Psi + \sum_{k>0} \phi_k(\mathbf{r}) \hat{a}_k.$$

In the low-temperature limit we can neglect the higher states due to their low occupancy and write the field operator as a classical field  $\Psi \in \mathbb{C}$ . The term “classical field” has its origin in the close analogy to the treatment of a classical light field in quantum electrodynamics. The field operator is now simply given by  $\hat{\Psi} = \sqrt{N} \cdot \Psi$ .

Using this approximation we neglect all correlations between the atoms. The many-body problem (1.4) has therefore been reduced to an effective single-particle theory.

In the following we will call  $\Psi$  the wave function of the condensate<sup>8</sup>. It is important to note that it is not a wave function in a strict sense. In particular the equation of motion for  $\Psi$  can be non-linear. In the Heisenberg representation the dynamics of the system is described by

$$\begin{aligned} i\hbar \frac{\partial}{\partial t} \hat{\Psi} &= [\hat{\Psi}, \hat{H}] \\ &= \left[ -\frac{\hbar^2}{2m} \nabla^2 + V(\mathbf{r}) + \int d^3r' \hat{\Psi}^\dagger(\mathbf{r}') V_{\text{int}}(\mathbf{r}, \mathbf{r}') \hat{\Psi}(\mathbf{r}') \right] \hat{\Psi}. \end{aligned}$$

---

<sup>7</sup>This can be seen by looking at the action of the operators on Fock states:  $\hat{a}_0 |N, \dots\rangle = \sqrt{N} |N-1, \dots\rangle$  and  $\hat{a}_0^\dagger |N, \dots\rangle = \sqrt{N+1} |N+1, \dots\rangle$

<sup>8</sup>It is also called the order parameter of the condensate to stress the connection to the thermodynamics of phase transitions. In the BEC phase there is a symmetry breaking due to the global phase

Inserting  $\hat{\Psi} = \sqrt{N} \cdot \Psi$  and the low temperature limit for the contact interaction potential (1.1) leads to the equation of motion for the condensate wave function<sup>9</sup>

$$i\hbar \frac{\partial}{\partial t} \Psi(\mathbf{r}, t) = \left[ -\frac{\hbar^2}{2m} \nabla^2 + V(\mathbf{r}) + gN |\Psi|^2 \right] \Psi(\mathbf{r}, t). \quad (1.5)$$

Equation (1.5) is called Gross-Pitaevskii equation. There are different conventions in writing it down. First, we have chosen to keep  $\Psi$  normalized to unity in order to keep track of the dependence on the number of atoms. Second, since one particle is interacting with  $N - 1$  others, the factor  $N$  is often replaced by  $N - 1$ . For reasons of brevity and since  $N \gg 1$  we keep the short form here. Due to the normalization the density of the condensate is given by

$$n(\mathbf{r}) = N |\Psi(\mathbf{r})|^2.$$

Analogous to the Schrödinger equation one can derive the stationary form of the Gross-Pitaevskii equation by setting

$$\Psi(\mathbf{r}, t) = \Psi(\mathbf{r}) \exp\left(-\frac{i}{\hbar} \mu t\right),$$

where the energy  $\mu$  is the chemical potential. This yields the time-independent or stationary form of the Gross-Pitaevskii equation

$$\mu \Psi(\mathbf{r}) = \left[ -\frac{\hbar^2}{2m} \nabla^2 + V(\mathbf{r}) + gN |\Psi|^2 \right] \Psi(\mathbf{r}). \quad (1.6)$$

### 1.3.2. Mean-field description including dipolar interactions

The addition of the dipolar interaction to the Gross-Pitaevskii equation is straightforward [23, 24] (see [20, chapter 4.2] for a detailed discussion of the validity). The dipolar interaction potential is treated in the same way as the contact interaction  $\delta$ -potential:

$$\begin{aligned} i\hbar \frac{\partial}{\partial t} \Psi(\mathbf{r}, t) = & \left[ -\frac{\hbar^2}{2m} \nabla^2 + V(\mathbf{r}) + gN |\Psi(\mathbf{r}, t)|^2 \right. \\ & \left. + \frac{3}{4\pi} g_{\text{dd}} N \int d^3 r' \frac{1 - 3 \cos^2(\vartheta)}{|\mathbf{r} - \mathbf{r}'|^3} |\Psi(\mathbf{r}', t)|^2 \right] \Psi(\mathbf{r}, t). \end{aligned} \quad (1.7)$$

We introduce a mean-field interaction potential for the dipolar part [25]

$$\Phi_{\text{dd}}(\mathbf{r}, t) = \frac{3}{4\pi} g_{\text{dd}} N \int d^3 r' \frac{1 - 3 \cos^2(\vartheta)}{|\mathbf{r} - \mathbf{r}'|^3} |\Psi(\mathbf{r}', t)|^2.$$

Note that this depends on the wave function  $\Psi$  and therefore also on time. With this definition, equation (1.7) gives

$$i\hbar \frac{\partial}{\partial t} \Psi(\mathbf{r}, t) = \left[ -\frac{\hbar^2}{2m} \nabla^2 + V(\mathbf{r}) + gN |\Psi(\mathbf{r}, t)|^2 + \Phi_{\text{dd}}(\mathbf{r}, t) \right] \Psi(\mathbf{r}, t). \quad (1.8)$$

---

<sup>9</sup>Dipolar interactions will be added in the next section.

**Energy functional:** As we will be using the variational principle to find approximate ground states of the system described by the Gross-Pitaevskii equation, we also need the energy (per particle) of a given condensate wave function  $\Psi(\mathbf{r})$ . It is given by [16, 18]

$$E[\Psi]/N = \int d^3r \left[ \frac{\hbar^2}{2m} |\nabla \Psi|^2 + V(\mathbf{r}) |\Psi|^2 + \frac{1}{2} g N |\Psi|^4 + \frac{1}{2} \Phi_{\text{dd}}(\mathbf{r}) |\Psi(\mathbf{r})|^2 \right]. \quad (1.9)$$

It is readily obtained by inserting  $\hat{\Psi} = \sqrt{N} \cdot \Psi$  in the many-body Hamiltonian (1.4).

### 1.3.3. Dimensionless form of the Gross-Pitaevskii equation

Dimensionless forms of physical theories allow for a deeper understanding of the system. By choosing appropriate units the equations can be simplified and the important parameters and scaling relations may be identified.

In the following we will derive a dimensionless form of the Gross-Pitaevskii equation by rescaling to dimensionless variables  $\tilde{\mathbf{r}}, \tilde{t}, \dots$  using  $\lambda, \tau, \epsilon$  as units for length, time and energy, respectively. The single quantities transform according to the rules

$$\begin{aligned} \mathbf{r} &\longrightarrow \lambda \cdot \tilde{\mathbf{r}} & V &\longrightarrow \epsilon \cdot \tilde{V} \\ t &\longrightarrow \tau \cdot \tilde{t} & \Psi &\longrightarrow \lambda^{-\frac{3}{2}} \cdot \tilde{\Psi} \\ \nabla^2 &\longrightarrow \lambda^{-2} \cdot \tilde{\nabla}^2 & \partial_t &\longrightarrow \tau^{-1} \partial_{\tilde{t}} \\ a &\longrightarrow \lambda \cdot \tilde{a} & a_{\text{dd}} &\longrightarrow \lambda \cdot \tilde{a}_{\text{dd}} \\ g &\longrightarrow \lambda^3 \epsilon \cdot \tilde{g} & g_{\text{dd}} &\longrightarrow \lambda^3 \epsilon \cdot \tilde{g}_{\text{dd}}. \end{aligned}$$

Equation (1.7) then reads

$$\begin{aligned} i\hbar \frac{\lambda^{-\frac{3}{2}}}{\tau} \frac{\partial}{\partial \tilde{t}} \tilde{\Psi} = & \left[ -\frac{\hbar^2}{2m\lambda^2} \tilde{\nabla}^2 + \epsilon \tilde{V}(\mathbf{r}) + \frac{4\pi\hbar^2 \tilde{a} \lambda}{m\lambda^3} N |\tilde{\Psi}|^2 \right. \\ & \left. + \frac{3}{4\pi} \frac{4\pi\hbar^2 \tilde{a}_{\text{dd}} \lambda}{m\lambda^3} N \int d^3\tilde{\mathbf{r}}' \frac{1 - 3\cos^2(\vartheta)}{|\tilde{\mathbf{r}} - \tilde{\mathbf{r}}'|^3} |\tilde{\Psi}(\tilde{\mathbf{r}}')|^2 \right] \lambda^{-\frac{3}{2}} \tilde{\Psi}. \end{aligned}$$

By choosing the following energy and time units<sup>10</sup>

$$\epsilon \equiv \frac{\hbar^2}{m\lambda^2} \quad \tau \equiv \frac{m\lambda^2}{\hbar}$$

we end up at ( $\tilde{g} = 4\pi\tilde{a}$  and  $\tilde{g}_{\text{dd}} = 4\pi\tilde{a}_{\text{dd}}$ )

$$\begin{aligned} i \frac{\partial}{\partial \tilde{t}} \tilde{\Psi} = & \left[ -\frac{1}{2} \tilde{\nabla}^2 + \tilde{V}(\tilde{\mathbf{r}}) + \tilde{g} N |\tilde{\Psi}|^2 \right. \\ & \left. + \frac{3}{4\pi} \tilde{g}_{\text{dd}} N \int d^3\tilde{\mathbf{r}}' \frac{1 - 3\cos^2(\vartheta)}{|\tilde{\mathbf{r}} - \tilde{\mathbf{r}}'|^3} |\tilde{\Psi}(\tilde{\mathbf{r}}', t)|^2 \right] \tilde{\Psi}. \end{aligned} \quad (1.10)$$

---

<sup>10</sup>Note that we are not making any assumptions in this step. Any other  $\epsilon$  and  $\tau$  can be chosen as long as they have units of energy and time.



The only two parameters left—besides the ones for the specific external potential—are  $\tilde{g}N$  and  $\tilde{g}_{\text{dd}}N$ , two dimensionless values determining the strength of the different interaction types. The dimensionless form of the energy functional (1.9) is given by

$$\tilde{E}[\tilde{\Psi}] = \int d^3\tilde{r} \left[ \frac{1}{2} |\tilde{\nabla}\tilde{\Psi}|^2 + \tilde{V}(\tilde{\mathbf{r}}) |\tilde{\Psi}|^2 + \frac{1}{2} \tilde{g}N |\tilde{\Psi}|^4 + \frac{1}{2} \tilde{\Phi}_{\text{dd}}(\tilde{\mathbf{r}}) |\tilde{\Psi}|^2 \right]. \quad (1.11)$$

We are still free to choose a length scale. This will help to simplify the formulas for the different external potentials. We will discuss two examples in the following paragraphs, the harmonic potential and the Gaussian multi-well potential. Both will be used throughout this thesis. It is also possible to take one of the two lengths  $a$  or  $a_{\text{dd}}$ , thereby fixing one of the coupling constants to  $4\pi$ .

When later referring to equations (1.10), (1.11) we will just skip the notation with the tilde and use the normal symbols for the dimensionless quantities.

### Harmonic potential

For an external harmonic potential with trapping frequencies  $\omega_i$  for the different spatial directions we have

$$\begin{aligned} \tilde{V} = \frac{V}{\epsilon} &= \frac{m\lambda^2}{\hbar^2} \times \frac{m}{2} \sum_i \omega_i^2 x_i^2 \\ &= \frac{1}{2} \sum_i \frac{m^2 \lambda^4}{\hbar^2} \omega_i^2 \tilde{x}_i^2. \end{aligned}$$

Now the length scale  $\lambda$  may be chosen to be the harmonic oscillator length for one of the frequencies, say  $z$

$$\lambda \equiv \sqrt{\frac{\hbar}{m\omega_z}}$$

leading to

$$\tilde{V} = \frac{1}{2} \left( \left( \frac{\omega_x}{\omega_z} \right)^2 \tilde{x}^2 + \left( \frac{\omega_y}{\omega_z} \right)^2 \tilde{y}^2 + \tilde{z}^2 \right).$$

### Multi-well potential

For the Gaussian multi-well potential with  $N_S$  wells, depth  $V_0$ , different trap widths  $w_i$  and lattice spacing  $l$  in  $z$ -direction (for details see chapter 2.1)

$$V = -V_0 \sum_{s=-N_S/2}^{N_S/2} \exp \left( -\frac{2x^2}{w_x^2} - \frac{2y^2}{w_y^2} - \frac{2(z - s \cdot l)^2}{w_z^2} \right)$$

it turns out to be convenient to choose the lattice spacing as the length scale ( $\lambda \equiv l$ ) which leads to the dimensionless form

$$\tilde{V} = -\tilde{V}_0 \sum_s \exp \left( -\frac{2\tilde{x}^2}{\tilde{w}_x^2} - \frac{2\tilde{y}^2}{\tilde{w}_y^2} - \frac{2(\tilde{z} - s)^2}{\tilde{w}_z^2} \right),$$

where  $\tilde{V}_0 = V_0/\epsilon$  is the dimensionless depth.

### 1.3.4. Approximate solutions in a harmonic trap

We briefly review the solutions of the stationary Gross-Pitaevskii equation in some limiting cases. We will use the results (Gaussian and inverted parabolic density distributions) for different calculations throughout the next chapters.

In the *dimensionless* form, for a spherical harmonic trap, the dipolar Gross-Pitaevskii equation reads

$$\mu\Psi = \left[ -\frac{1}{2}\nabla^2 + \frac{1}{2}r^2 + gN|\Psi|^2 + \Phi_{\text{dd}}(\mathbf{r}) \right] \Psi. \quad (1.12)$$

#### Non-interacting

For an ideal gas without any interactions we have  $g = 0$  and  $g_{\text{dd}} = 0$  and recover the Schrödinger equation for a harmonic oscillator:

$$\mu\Psi = \left[ -\frac{1}{2}\nabla^2 + \frac{1}{2}r^2 \right] \Psi.$$

The ground state wave function is simply given by a Gaussian wave function

$$\Psi(\mathbf{r}) = \frac{1}{\pi^{3/4}} e^{-r^2/2}.$$

Remember that lengths are measured in units of the harmonic oscillator length  $a_{\text{HO}} = \sqrt{\hbar/m\omega}$ .

#### Strongly interacting (contact interaction only)

For strong interactions, if  $Na/a_{\text{HO}} \gg 1$ , it can be shown that the kinetic energy may be neglected [17, chapter 3]. This is called Thomas-Fermi approximation. Within this regime, equation (1.12) transforms into a simple algebraic equation:

$$\mu\Psi = \left[ \frac{1}{2}r^2 + gN|\Psi|^2 \right] \Psi. \quad (1.13)$$

Dividing by  $\Psi$  and solving for the density  $n(\mathbf{r}) = N|\Psi(\mathbf{r})|^2$  leads to an inverted parabola as a solution<sup>11</sup>

$$n(\mathbf{r}) = \frac{\mu}{g} \left( 1 - \frac{r^2}{2\mu} \right).$$

---

<sup>11</sup>This solution is only correct for positive values of the density,  $r < \sqrt{2\mu}$ .

## Strongly interacting

Adding dipolar interactions within the Thomas-Fermi approximation turns the Gross-Pitaevskii equation into an integral equation

$$\mu = \left[ \frac{1}{2} r^2 + g \cdot n(\mathbf{r}) + \frac{3}{4\pi} g_{\text{dd}} N \int d^3 r' \frac{1 - 3 \cos^2(\vartheta)}{|\mathbf{r} - \mathbf{r}'|^3} n(\mathbf{r}') \right].$$

Surprisingly, the solution is still parabolic, though with changed aspect ratios of the wave function (see [26] for details). In general, dipolar condensates elongate in the direction of the polarization axis. This is a direct consequence of the lowering in energy due to the head-to-tail configuration of the dipoles ( $\rightarrow\rightarrow$ ).

Note that the Thomas-Fermi condition in the dipolar case is depending on the dipolar length  $a_{\text{dd}}$  and the trap geometry [25, section 2.3.4].

## 1.4. Basic properties

### 1.4.1. Stability of dipolar quantum gases

Quantum gases can become unstable and undergo a collapse if the interaction between the particles reaches a certain strength which depends on the external parameters. Typically a critical scattering length  $a_{\text{crit}}$  is defined below which the condensate is unstable. For purely contact interacting gases in a spherical harmonic trap with an oscillator length of  $a_{\text{HO}} = \sqrt{\hbar/m\omega}$  this value<sup>12</sup> is given by [19, chapter 5.2]

$$\frac{a_{\text{crit}} N}{a_{\text{HO}}} \approx -0.57.$$

For large particle numbers  $N$ , the critical scattering length goes to zero.

For dipolar condensates the stability condition is more complex since it depends on the polarization axis, the strength of the dipolar interaction and the geometry of the trapping potential [8]. We will only consider a simplified case here. We assume that the system is rotationally symmetric with respect to the polarization axis (say,  $z$ ). Let the trapping frequency in the radial direction be  $\omega_\rho$  and the  $z$ -frequency  $\omega_z$ . Assuming a Gaussian wave function with radial width  $\sigma_\rho$  and axial width  $\sigma_z$ , the energy of the condensate in the limit of large  $N$  is given by (see section 2.3 for a complete derivation and the definition<sup>13</sup> of  $f_{\text{dip}}$ )

$$E = \frac{N^2}{\sqrt{2\pi}\sigma_\rho^2\sigma_z} (a - a_{\text{dd}} \cdot f_{\text{dip}}(\kappa)),$$

<sup>12</sup>The numerical constant on the right side of the condition is slightly modified if the trap aspect ratio changes [27].

<sup>13</sup>The function  $f_{\text{dip}}$  is defined in equation (2.6).

where  $\kappa = \sigma_\rho/\sigma_z$  is the aspect ratio of the cloud and  $f_{\text{dip}}(\kappa)$  is a monotonically decreasing function with values between 1 and  $-2$ . The critical scattering length of the condensate is now given by (see [25, section 4.2] for the full reasoning)

$$a_{\text{crit}} = a_{\text{dd}} \cdot f_{\text{dip}}(\kappa).$$

This is only an implicit equation for  $a_{\text{crit}}$  since the aspect ratio  $\kappa$  itself is a function of  $a_{\text{dd}}/a$  and the trap aspect ratio  $\omega_z/\omega_\rho$ .

Nevertheless we can make some simple statements about the stability by assuming that the ratio  $\kappa$  is given<sup>14</sup>. The function  $f_{\text{dip}}$  has the property  $f_{\text{dip}}(1) = 0$ . Since it is monotonically decreasing this leads to the conclusion that traps which force the dipolar cloud to be prolate with an aspect ratio  $\kappa < 1$  are destabilizing. This should be understood in the sense that the system has a positive critical scattering length which increases with  $a_{\text{dd}}$ . In contrast, traps which force the condensate to be oblate<sup>15</sup> ( $\kappa > 1$ ) are stabilizing which means that the system has a critical scattering length that can be significantly smaller than zero (the lowest  $a_{\text{crit}}$  is given by  $-2a_{\text{dd}}$  due to the properties of  $f_{\text{dip}}$ ).

The stability criterion has to be modified for condensates which are not rotationally symmetric with respect to the polarization axis [28]. In general it is true that a compression of the cloud in the polarization direction or a decompression perpendicular to it stabilizes the system [25, chapter 7]. We will make use of this property in section 6.3.

### 1.4.2. Fourier transform of the dipolar potential

Fourier transformations are introduced in this section for two reasons. For both analytical calculations and numerical simulations it is useful to derive the Fourier transform of the dipolar interaction term in the Gross-Pitaevskii equation (1.10) as it has the form of a convolution which can easily be evaluated in  $k$ -space.

To see this, note first that with

$$\begin{aligned} \cos(\vartheta) &= \frac{\boldsymbol{\mu} \cdot (\mathbf{r} - \mathbf{r}')}{|\boldsymbol{\mu} \cdot (\mathbf{r} - \mathbf{r}')|} \\ r &= |\mathbf{r} - \mathbf{r}'| \end{aligned}$$

$V_{\text{dd}}(\mathbf{r}, \mathbf{r}')$  from equation (1.3) is only depending on the difference  $\mathbf{r} - \mathbf{r}'$ . With the interaction part  $\Phi_{\text{dd}}(\mathbf{r})$  and the density  $n(\mathbf{r}) = N |\Psi|^2$  one may write

$$\begin{aligned} \Phi_{\text{dd}}(\mathbf{r}) &= \frac{3}{4\pi} g_{\text{dd}} N \int d^3 r' \frac{1 - 3 \cos^2(\vartheta)}{|\mathbf{r} - \mathbf{r}'|^3} |\Psi(\mathbf{r}')|^2 \\ &= \int d^3 r' V_{\text{dd}}(\mathbf{r} - \mathbf{r}') n(\mathbf{r}') \\ &\equiv (V_{\text{dd}} \star n)(\mathbf{r}) \end{aligned} \tag{1.14}$$

---

<sup>14</sup>For the non-interacting case it is given by  $\kappa = \sqrt{\omega_z/\omega_\rho}$ . In the Thomas-Fermi regime without dipolar interactions the aspect ratio is given by  $\kappa = \omega_z/\omega_\rho$ . An expression for the dipolar case exists, too [25, section 2.3.4]

<sup>15</sup>They need to be oblate at scattering length  $a = 0$ .

which is the convolution of the dipolar potential with the density. Using the following convention for the  $d$ -dimensional Fourier transform and its inverse

$$\begin{aligned}\mathcal{F}\{f(\mathbf{r})\} &= \int \frac{d^d r}{(2\pi)^{d/2}} f(\mathbf{r}) e^{-i\mathbf{k}\mathbf{r}} \\ \mathcal{F}^{-1}\{f(\mathbf{k})\} &= \int \frac{d^d k}{(2\pi)^{d/2}} f(\mathbf{k}) e^{i\mathbf{k}\mathbf{r}}\end{aligned}$$

we can use the convolution theorem to calculate the Fourier transform of  $\Phi_{\text{dd}}$ . A convolution in coordinate space is represented by a product in Fourier space:

$$\mathcal{F}\{\Phi_{\text{dd}}\} = \mathcal{F}\{V_{\text{dd}} \star n\} = (2\pi)^{3/2} \cdot \mathcal{F}\{V_{\text{dd}}\} \cdot \mathcal{F}\{n\}.$$

The Fourier transform  $\mathcal{F}\{V_{\text{dd}}\}$  of the dipolar potential is given by<sup>16</sup> [24, 25]

$$\mathcal{F}\{V_{\text{dd}}\}(\mathbf{k}) = \frac{3 \cdot g_{\text{dd}}}{(2\pi)^{3/2}} (1 - 3 \cos^2(\alpha)) \left[ \frac{\cos(kb)}{(kb)^2} - \frac{\sin(kb)}{(b)^3} \right].$$

Here  $b$  is a short distance cut-off<sup>17</sup> which has to be introduced to regularize the 3D integration at  $r = 0$  and  $\alpha$  is the angle between  $\boldsymbol{\mu}$  and  $\mathbf{k}$ . In the limit  $b \rightarrow 0$  the Fourier transform can be simplified to

$$\mathcal{F}\{V_{\text{dd}}\}(\mathbf{k}) = -\frac{g_{\text{dd}}}{(2\pi)^{3/2}} (1 - 3 \cos^2(\alpha)). \quad (1.15)$$

---

<sup>16</sup>Note that we use the symmetric form of the Fourier transformation, therefore there is an additional factor of  $(2\pi)^{-3/2}$ .

<sup>17</sup>A small sphere with radius  $b$  around the origin is cut from the whole integral. The integral over this small sphere ( $kb \ll 1$  such that the exponential factor is essentially 1) gives zero, since  $\int d^3r \frac{1-3\cos^2(\theta)}{r^3} = 0$ . Note that there is also a natural cut-off at small distances due to the finite size of an atom.



## 2. Multi-well physics

The idea to load a quantum gas into several potential wells has existed for quite some time and was first realized only two years after the achievement of the first Bose-Einstein condensate [29]. There are several motivations to do this. The first experiments on the double-well were mostly focused on the link between two macroscopic quantum objects. The analogy to the Josephson junction in superconductors is obvious. Indeed there are numerous studies on the Josephson physics [30, 31].

The second motivation is also linked to solid state physics. A multi-well system can be a minimal model system for a crystalline structure. While optical lattices form a large periodic array, the multi-well system is suited to focus on a few single wells and to study the interaction between neighboring ones. To enhance the interaction between different wells we will typically consider mesoscopic samples of a few thousand particles per site.

This chapter will give an introduction to some aspects of the multi-well physics of dipolar quantum gases.

### 2.1. Multi-well potentials

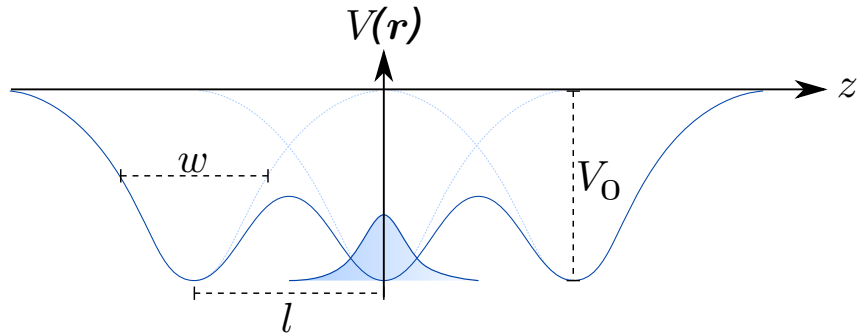


**Figure 2.1.:** The geometry of a Gaussian multi-well potential (here: cut through triple-well potential along the symmetry axis). The spacing between the wells is  $l$ , the axial width of the Gaussians is  $w$  and the depth of the wells is  $V_0$ . Note:  $V_0$  is *not* the height of the barrier between two wells.

Most of the models presented in this work will not depend on the actual geometry of the multi-well potential. For the numerical simulations presented in chapter 6 though, we have to define an explicit shape of the potential. We will use a Gaussian multi-well

potential as it matches most closely the planned experimental realization (see [15, chapter 4] and appendix A). For  $N_S$  wells in  $z$ -direction we define the potential<sup>1</sup>

$$V(\mathbf{r}) = -V_0 \sum_{s=-N_S/2}^{N_S/2} \exp\left(-\frac{2x^2}{w_x^2} - \frac{2y^2}{w_y^2} - \frac{2(z - s \cdot l)^2}{w_z^2}\right).$$

The parameter  $V_0$  determines the center depth of the individual wells and the widths  $w_i$  parametrize the geometry of a single well (size in each direction). The spacing between the wells (“lattice spacing”) is given by  $l$ .

### Harmonic approximation of the Gaussian multi-well potential

In the center  $|x_i| \ll w_i$  of a single well (take the one with  $s = 0$ ) the potential can be approximated by a harmonic potential

$$V(\mathbf{r}) \approx -V_0 \left(1 - \sum_{i=1}^3 \frac{2x_i^2}{w_i^2}\right) = -V_0 + \frac{m}{2} \sum_{i=1}^3 \omega_i^2 x_i^2,$$

where the trap frequencies  $\omega_i$  are given by  $\omega_i^2 = 4V_0/mw_i^2$ . We use this approximation only to switch between the two pictures (Gaussian potential and harmonic potential). For some analytic calculations we use the harmonic potential (chapter 5) but for the simulations (chapter 6) the full Gaussian multi-well potential is used.

## 2.2. Inter-site energy

The long-ranging dipolar interactions lead to a new aspect in the multi-well system compared to purely contact interacting gases: neighboring wells are interacting with each other (without interchange of particles). Also wells which are further apart are influenced by the dipolar repulsion or attraction. In a first estimation this interaction should fall off with the distance  $l$  like  $l^{-3}$ . However, this is only correct for very tightly localized wave functions.

To estimate the dipolar inter-site interaction energy in a more realistic case, the following simplified scenario is considered. Two cylindrically symmetric wave functions of Gaussian type<sup>2</sup> are separated by a distance  $l$ . Both have the same number of atoms  $N$  and we consider the polarization axis to match with the symmetry axis ( $\rightarrow\rightarrow$  configuration).

---

<sup>1</sup>The placement of the 2 into the numerator is used because the different  $w_i$  can directly be identified with the width of a Gaussian laser beam [32, chapter 4]

<sup>2</sup>We use Gaussian wave functions as an approximate solution within the single wells, see section 1.3.4 for details.



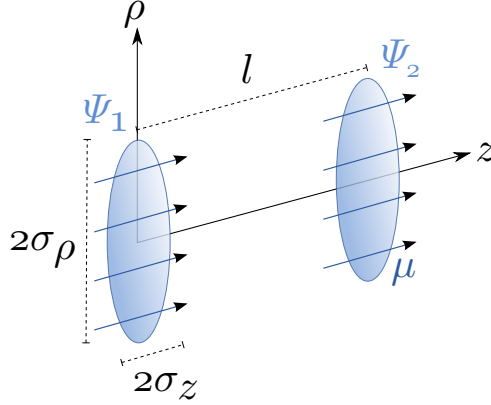


**Figure 2.2.:** Sketch of the geometry for the calculation of the inter-site energy. Two Gaussian wave functions with widths  $\sigma_z$  in axial and  $\sigma_\rho$  in radial direction are separated by a distance  $l$ . The polarization axis matches with the symmetry axis  $z$ .

We define the wave functions in the single wells by

$$\begin{aligned}\Psi_1(\mathbf{r}) &= \frac{1}{\pi^{3/4}\sigma_\rho\sqrt{\sigma_z}} \exp\left(-\frac{\rho^2}{2\sigma_\rho^2} - \frac{z^2}{2\sigma_z^2}\right), \\ \Psi_2(\mathbf{r}) &= \frac{1}{\pi^{3/4}\sigma_\rho\sqrt{\sigma_z}} \exp\left(-\frac{\rho^2}{2\sigma_\rho^2} - \frac{(z-l)^2}{2\sigma_z^2}\right).\end{aligned}$$

The corresponding densities are

$$n_i(\mathbf{r}) = \frac{N}{\pi^{3/2}\sigma_\rho^2\sigma_z} \exp\left(-\frac{\rho^2}{\sigma_\rho^2} - \frac{(z-\delta_i)^2}{\sigma_z^2}\right),$$

where we have set the displacement  $\delta_1 = 0$  and  $\delta_2 = l$ . We assume that the spacing  $l$  is several times larger than the axial width of the wave function  $\sigma_z$  such that the overlap of  $\Psi_1(\mathbf{r})$  and  $\Psi_2(\mathbf{r})$  is negligible.

The whole system is described by the function  $\Psi(\mathbf{r}) = \Psi_1(\mathbf{r}) + \Psi_2(\mathbf{r})$ . According to equation (1.9), the total dipolar energy is then given by

$$\begin{aligned}E_{\text{dipolar}} &= \frac{N^2}{2} \int d^3r \int d^3r' |\Psi(\mathbf{r})|^2 V_{\text{dd}}(\mathbf{r}, \mathbf{r}') |\Psi(\mathbf{r}')|^2 \\ &= \frac{N^2}{2} \int d^3r \int d^3r' |\Psi_1(\mathbf{r}) + \Psi_2(\mathbf{r})|^2 V_{\text{dd}}(\mathbf{r}, \mathbf{r}') |\Psi_1(\mathbf{r}') + \Psi_2(\mathbf{r}')|^2 \\ &\approx \underbrace{\frac{1}{2} \int d^3r \int d^3r' n_1(\mathbf{r}) V_{\text{dd}}(\mathbf{r}, \mathbf{r}') n_1(\mathbf{r}')}_{\equiv E_{\text{on-site}}} + \underbrace{\frac{1}{2} \int d^3r \int d^3r' n_2(\mathbf{r}) V_{\text{dd}}(\mathbf{r}, \mathbf{r}') n_2(\mathbf{r}')}_{\equiv E_{\text{on-site}}} \\ &\quad + \underbrace{\int d^3r \int d^3r' n_1(\mathbf{r}) V_{\text{dd}}(\mathbf{r}, \mathbf{r}') n_2(\mathbf{r}')}_{\equiv E_{\text{int}}} \\ &= 2 \cdot E_{\text{on-site}} + E_{\text{int}},\end{aligned}\tag{2.1}$$

where we have used the symmetry between  $n_1$  and  $n_2$  and the vanishing of the overlap. Note that we count the inter-site energy only once for each pair of condensates.

Using the convolution theorem twice, the inter-site energy can be written in terms of the Fourier transforms<sup>3</sup>

$$E_{\text{int}} = (2\pi)^{3/2} \int d^3k \mathcal{F}\{n_1\} \cdot \mathcal{F}\{V_{\text{dd}}\} \cdot \mathcal{F}\{n_2\}.$$

The Fourier transform of the density gives ( $k_\rho^2 = k_x^2 + k_y^2$ )

$$\mathcal{F}\{n_i\} = \frac{N}{(2\pi)^{3/2}} \exp\left(-\frac{1}{4}k_\rho^2\sigma_\rho^2 - \frac{1}{4}k_z^2\sigma_z^2 - i\delta_i k_z\right).$$

Note that the displacement in coordinate space leads to the phase shift in Fourier space. As we know the Fourier transform of all three parts we have already reduced the problem from six to three integrations. For the Fourier transform of the dipolar potential (1.15) we set  $\cos(\alpha) = \hat{\mathbf{k}} \cdot \mathbf{e}_z = \frac{k_z}{k}$  and thus

$$\mathcal{F}\{V_{\text{dd}}\} = -\frac{g_{\text{dd}}}{(2\pi)^{3/2}} \left(1 - 3\frac{k_z^2}{k^2}\right).$$

Putting everything together, we get the following expression for the interaction energy:

$$E_{\text{int}} = -\frac{g_{\text{dd}}N^2}{(2\pi)^3} \int d^3k \left(1 - 3\frac{k_z^2}{k^2}\right) \exp\left(-\frac{1}{2}k_\rho^2\sigma_\rho^2 - \frac{1}{2}k_z^2\sigma_z^2 - ilk_z\right).$$

Changing the integration variable to the dimensionless  $\mathbf{q} = \sigma_\rho \cdot \mathbf{k}$ , defining the ratio  $\kappa = \sigma_\rho/\sigma_z$  and the dimensionless distance  $\lambda = l/\sigma_\rho$  this transforms to

$$E_{\text{int}} = -\frac{g_{\text{dd}}N^2}{(2\pi)^3\sigma_\rho^3} \int d^3q \left(1 - 3\frac{q_z^2}{q^2}\right) \exp\left(-\frac{1}{2}q_\rho^2 - \frac{1}{2}q_z^2\kappa^{-2} - i\lambda q_z\right).$$

Now we use spherical coordinates  $q, \vartheta, \varphi$  for the  $q$ -integration. We set  $u \equiv \cos(\theta)$  and perform the  $\varphi$  integration which gives simply  $2\pi$ :

$$E_{\text{int}} = -\frac{g_{\text{dd}}N^2 \cdot 2\pi}{(2\pi)^3\sigma_\rho^3} \int_0^\infty dq \int_{-1}^1 du q^2 (1 - 3u^2) \exp\left(-\frac{1}{2}q^2 \left((1 - u^2) + \kappa^{-2}u^2\right) - i\lambda qu\right).$$

The  $q$  integration can be performed analytically leading to

$$E_{\text{int}} = -\frac{g_{\text{dd}}N^2}{(2\pi)^{3/2}\sigma_\rho^3} \int_0^1 du \frac{(1 - 3u^2)(1 - u^2(\eta + \lambda^2))}{(1 - \eta u^2)^{5/2}} \exp\left(-\frac{\lambda^2 u^2}{2(1 - \eta u^2)}\right). \quad (2.2)$$

Here we have used  $\eta = 1 - \kappa^{-2}$ . The  $u$ -integration domain has been changed to the interval from 0 to 1 using the even symmetry. This is our final result for the inter-site energy. It matches the expression of [33]. The integration which is left has to be performed numerically.

---

<sup>3</sup>Note that there is a factor of  $(2\pi)^{-3/2}$  for the three Fourier transforms and a factor of  $(2\pi)^3$  for each of the representations of the two  $\delta$  functions:  $\delta(\mathbf{k} - \mathbf{k}') = \frac{1}{(2\pi)^3} \int d^3r e^{i\mathbf{r}(\mathbf{k} - \mathbf{k}')}.$  We have also used that  $\mathcal{F}\{n_1\}(-\mathbf{k}) = \mathcal{F}\{n_1\}(\mathbf{k})$ .

### 2.2.1. Limiting cases

To get some insight into the result of equation (2.2) we introduce a slightly different notion and specify to some limiting cases.

If each cloud would be contracted to a single point ( $\delta$ -function as density) the interaction energy would match with the energy of two head-to-tail dipoles at a distance  $l$  (times  $N^2$ ). We define this energy as

$$E_\delta \equiv \frac{3}{4\pi} g_{\text{dd}} \frac{(-2)}{l^3} \cdot N^2 = -\frac{3g_{\text{dd}}N^2}{2\pi l^3}.$$

With this definition we can restate the inter-site energy  $E_{\text{int}} \equiv G(\eta, \lambda)E_\delta$  in terms of a dimensionless function given by

$$\begin{aligned} E_{\text{int}}/E_\delta &= \frac{\lambda^3}{3\sqrt{2\pi}} \int_0^1 du \frac{(1-3u^2)(1-u^2(\eta+\lambda^2))}{(1-\eta u^2)^{5/2}} \exp\left(-\frac{\lambda^2 u^2}{2(1-\eta u^2)}\right) \\ &\equiv G(\eta, \lambda). \end{aligned} \quad (2.3)$$

The function  $G(\eta, \lambda)$  has the property (see figure 2.3(a) or spherical case below)

$$\lim_{\lambda \rightarrow \infty} G(\eta, \lambda) = 1 \quad (2.4)$$

which validates that for large distances ( $l \gg \sigma_\rho, \lambda \gg 1$ ) the interaction is not depending on the geometry of the cloud.

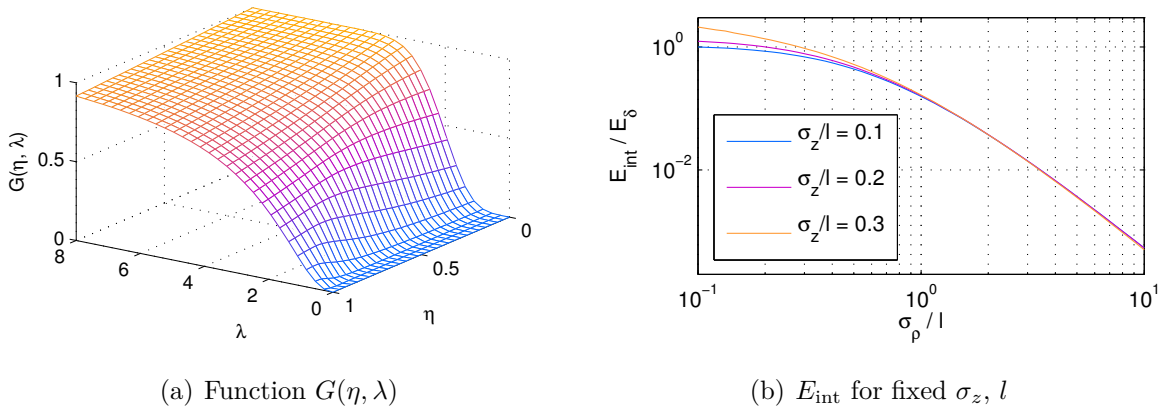


**Figure 2.3.:** (a) The function  $G(\eta, \lambda)$  for positive  $\eta$  (implying that  $\kappa > 1$ ). For  $\lambda \rightarrow \infty$  the function approaches a value of 1 meaning that the interaction becomes geometry independent ( $E_{\text{int}} \rightarrow E_\delta$ ). (b) Inter-site energy in units of  $E_\delta$  as a function of the radial size for different ratios of  $\sigma_z/l$ . The interaction energy grows if the radial size is reduced. For large  $\sigma_\rho/l$  this behavior is strong and scales like  $(\sigma_\rho/l)^{-3}$ .

**Spherical case:** In the spherical case ( $\sigma_\rho = \sigma_z, \kappa = 1, \eta = 0$ ) equation (2.3) simplifies to

$$G(0, \lambda) = -\frac{1}{3} e^{-\frac{\lambda^2}{2}} \lambda (3 + \lambda^2) \sqrt{\frac{2}{\pi}} + \operatorname{erf}\left(\frac{\lambda}{\sqrt{2}}\right).$$

In this special case it can directly be seen that property (2.4) is fulfilled as the error function goes to 1 in the limit  $\lambda \rightarrow \infty$ .

**Interaction energy for fixed  $\sigma_z$  and  $l$ :** Assuming that the two quantities  $\sigma_z$  and  $l$  are fixed, we can optimize  $\sigma_\rho$  to give a maximum inter-site energy which is most likely to yield strong dipolar effects. The energy is given by

$$E_{\text{int}} = E_\delta \cdot G\left(1 - \frac{\sigma_z^2}{\sigma_\rho^2}, \frac{l}{\sigma_\rho}\right),$$

where  $E_\delta$  is not depending on  $\sigma_\rho$ . Figure 2.3(b) shows the ratio  $E_{\text{int}}/E_\delta$  as a function of  $\sigma_\rho/l$ . The interesting feature is that for large  $\sigma_\rho/l$  (small  $\lambda$ ) the interaction energy scales like  $E_{\text{int}} \propto \sigma_\rho^{-3}$ . For all  $\lambda$  it is true that the interaction energy is lowering with increasing  $\sigma_\rho$ . For  $\sigma_\rho \rightarrow \infty$  the interaction energy vanishes. This matches the calculation of the interaction energy between two thin dipolar discs of infinite extension in the radial direction which do not interact at all [34].

### 2.2.2. On-site energy as a special case

The on-site dipolar energy can also be extracted from equation (2.2). In the limit  $\lambda \rightarrow 0$  the two clouds are completely overlapping and the remaining integral can be evaluated analytically. According to the definition in equation (2.1), we have to introduce a factor of 1/2 for the on-site energy compared to the inter-site energy

$$\begin{aligned} E_{\text{on-site,dip}} &= \frac{1}{2} \lim_{\lambda \rightarrow 0} E_{\text{int}} = -\frac{g_{\text{dd}} N^2}{2(2\pi)^{3/2} \sigma_\rho^3} \int_0^1 du \frac{(1 - 3u^2)}{(1 - \eta u^2)^{3/2}} \\ &= -\frac{g_{\text{dd}} N^2}{2(2\pi)^{3/2} \sigma_\rho^3} \kappa f_{\text{dip}}(\kappa) \\ &= -\frac{g_{\text{dd}} N^2}{2(2\pi)^{3/2} \sigma_\rho^2 \sigma_z} f_{\text{dip}}(\kappa), \end{aligned} \tag{2.5}$$

where we have introduced (see [35] and [28, appendix A])

$$\begin{aligned} f_{\text{dip}}(\kappa) &\equiv \frac{1}{\kappa} \int_0^1 du \frac{(1 - 3u^2)}{(1 - (1 - \kappa^{-2})u^2)^{3/2}} \\ &= \frac{1 + 2\kappa^2}{1 - \kappa^2} - \frac{3\kappa^2 \operatorname{arctanh}(\sqrt{1 - \kappa^2})}{(1 - \kappa^2)^{3/2}}. \end{aligned} \tag{2.6}$$

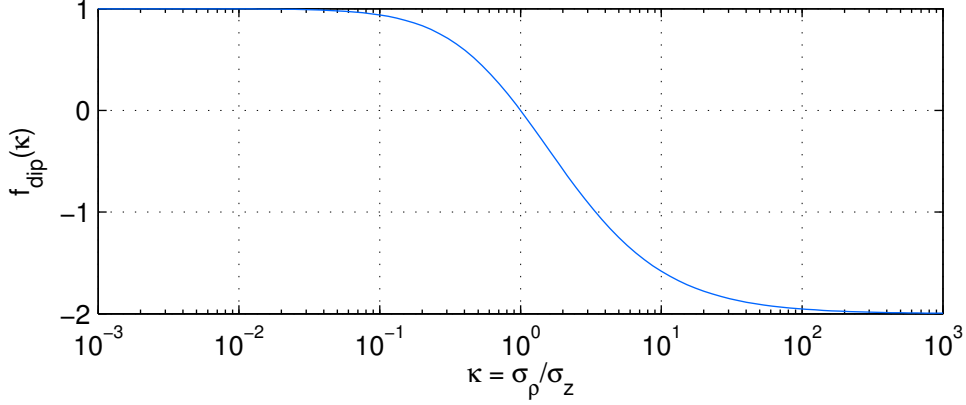


**Figure 2.4.:** The  $f_{\text{dip}}(\kappa)$  function for different aspect ratios  $\kappa = \sigma_\rho/\sigma_z$ . Values range from 1 for very prolate to  $-2$  for oblate clouds. The on-site energy (2.5) is thus negative (positive) for prolate (oblate) wave functions. For spherical clouds the dipolar energy vanishes:  $f_{\text{dip}}(1) = 0$ .

### 2.3. Energy functional for Gaussian wave functions

Having the dipolar on-site energy (2.5) it is straightforward to calculate the total energy for a Gaussian wave function. The result is useful as it is only depending on a few parameters and can be used for some simple estimations and variational calculations.

In the beginning we will assume that the trapping potential is a single harmonic well with radial symmetry<sup>4</sup> and trapping frequencies  $\omega_\rho, \omega_z$ . Inserting the function

$$\Psi(\mathbf{r}) = \frac{1}{\pi^{3/4} \sigma_\rho \sqrt{\sigma_z}} \exp\left(-\frac{\rho^2}{2\sigma_\rho^2} - \frac{z^2}{2\sigma_z^2}\right)$$

into the energy functional (1.9) leads to the expression

$$\frac{E_{\text{on-site}}}{N} = \frac{\hbar^2}{4m} \left( \frac{2}{\sigma_\rho^2} + \frac{1}{\sigma_z^2} \right) + \frac{m}{4} (2\omega_\rho^2 \sigma_\rho^2 + \omega_z^2 \sigma_z^2) + \frac{N}{2(2\pi)^{3/2} \sigma_\rho^2 \sigma_z} (g - g_{\text{dd}} f_{\text{dip}}(\kappa)).$$

The contact and the dipolar interaction exhibit the same scaling  $(\sigma_\rho^2 \sigma_z)^{-1}$ . The underlying reason is that both functions  $\delta(\mathbf{r})$  and  $1/r^3$  have the unit  $(\text{length})^{-3}$ .

The inter-site energy can be added as explained above, depending on how many wells are considered. Considering only two wells, each with  $N$  particles and a separation  $l = \lambda \sigma_\rho$ ,

<sup>4</sup>We derive a general version for the contact interacting case in  $d$  dimensions in chapter 5.2.

the total energy per particle is given by

$$\begin{aligned}\frac{E}{2N} &= \frac{1}{2N} (2E_{\text{on-site}} + E_{\text{int}}) \\ &= \frac{\hbar^2}{4m} \left( \frac{2}{\sigma_\rho^2} + \frac{1}{\sigma_z^2} \right) + \frac{m}{4} (2\omega_\rho^2 \sigma_\rho^2 + \omega_z^2 \sigma_z^2) \\ &\quad + \frac{N}{2(2\pi)^{3/2} \sigma_\rho^2 \sigma_z} \left( g - g_{\text{dd}} f_{\text{dip}}(\kappa) - g_{\text{dd}} \frac{\sqrt{2\pi}}{\lambda^3 \kappa} G(1 - \kappa^{-2}, \lambda) \right).\end{aligned}$$

This expression can be used to study the influence of the inter-site interaction on the wave functions in the single wells [36]. Also the stability of the overall condensate is significantly changed by inter-site effects (see [9] and [36, section 5.4] for a discussion within the Gaussian regime).

For our first approach to the dipolar multi-well system presented in the next chapter, the precise shape of the on-site wave functions is not of relevance. We will come back to the Gaussian wave functions in chapter 5, however.

## 3. Bose-Hubbard model

*Our first attempt to characterize the ground states of a dipolar quantum gas in a multi-well potential will make use of the Bose-Hubbard model which describes interacting bosonic particles in a periodic structure.*

*We will first give a brief introduction to the model and see how dipolar interactions can be included. Finally we apply the model to the case of a multi-well potential. We will see that the dipolar double-well can be mapped to the non-dipolar case. Therefore it yields no new features and henceforth we will use the triple-well to study a minimal dipolar multi-well system.*

*Studying this system will give some basic insights into the dipolar multi-well physics. Characteristic phases are appearing depending on the sign and value of the different energies involved, most prominently the on-site and inter-site interaction energy.*

### 3.1. Derivation

In the original work [37] and in most following publications [13, 38, 39] the Bose-Hubbard model is used to describe the physics of ultracold gases in optical lattices. Formed by a standing light field, they usually have several hundred filled lattice sites and may be one-, two- or three-dimensional. The usual filling rate is several atoms per site (to have on-site interactions there have to be at least two atoms).

The same model may also be applied to the case of the multi-well potential. However, the Bose-Hubbard model is an appropriate description only for a small filling factor, as we will see.

The starting point is the many-body Hamiltonian, considered already in section 1.3

$$\begin{aligned} \hat{H} = \int d^3r \, \hat{\Psi}^\dagger(\mathbf{r}) \left[ -\frac{\hbar^2}{2m} \nabla^2 + V(\mathbf{r}) \right] \hat{\Psi}(\mathbf{r}) \\ + \frac{1}{2} \int d^3r \int d^3r' \, \hat{\Psi}^\dagger(\mathbf{r}) \hat{\Psi}^\dagger(\mathbf{r}') V_{\text{int}}(\mathbf{r}, \mathbf{r}') \hat{\Psi}(\mathbf{r}') \hat{\Psi}(\mathbf{r}). \end{aligned} \quad (3.1)$$

The external potential is assumed to be periodic<sup>1</sup>. As a basis for the description we use again single-particle states. A particularly useful basis consists of states  $\phi(\mathbf{r})$  which are localized at a single well<sup>2</sup>. In the following we neglect all excited vibrational levels and

---

<sup>1</sup>It is enough to assume that the potential is periodic in a certain range such that the ground state wave functions in the outer wells are still approximately the same as for the inner wells.

<sup>2</sup>For an optical lattice with sinusoidal potential these are Wannier functions. But the exact shape is not of relevance for the derivation of the model.

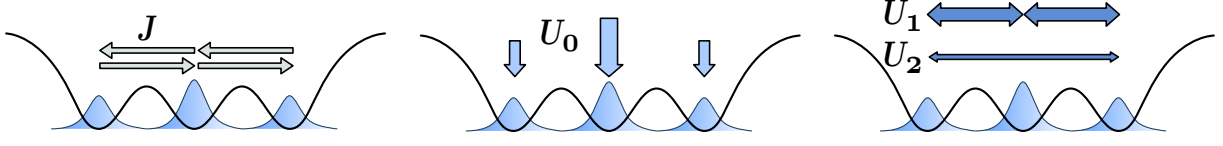


**Figure 3.1.:** The three important parameters in the Bose-Hubbard model: The tunneling constant  $J$ , the on-site energy  $U_0$  and the nearest-neighbor interaction energy  $U_1$ . The parameter  $U_2$  is depending on  $U_1$ , see text for further description.

therefore assume that the energies involved are small compared to the energy splitting between the ground state and excited states (this implies that the filling rate is low, otherwise the interaction energy is large enough to support excitations). If  $\phi_i(\mathbf{r})$  is the wave function centered at well  $i$  and  $N_S$  is the number of sites (wells), we can write

$$\hat{\Psi}(\mathbf{r}) = \sum_{i=1}^{N_S} \hat{a}_i \phi_i(\mathbf{r}).$$

Substituting this in equation (3.1) leads to the Bose-Hubbard Hamiltonian<sup>3</sup>

$$\hat{H} = -J \sum_{\langle i,j \rangle} \hat{a}_i^\dagger \hat{a}_j + \frac{U_0}{2} \sum_{i=1}^{N_S} \hat{n}_i (\hat{n}_i - 1) + \sum_{k=1}^{N_S-1} \left( U_k \sum_{\langle i,j \rangle_k} \hat{n}_i \hat{n}_j \right). \quad (3.2)$$

The  $\hat{a}_i^\dagger, \hat{a}_i, \hat{n}_i = \hat{a}_i^\dagger \hat{a}_i$  are the creation-, annihilation- and number operators at lattice site  $i$ , respectively. The energy parameters in this equation are the tunneling constant  $J$ , the on-site interaction energy  $U_0$  and the inter-site interaction energies  $U_1, U_2, \dots$  for the nearest, second-nearest,  $\dots$  neighbor, respectively. The brackets  $\langle i, j \rangle_k$  indicate the sum over the  $k$ -th nearest neighbors. We have assumed that the different sites are well separated.

The parameters  $J$  and  $U_0, U_1, \dots$  depend on the single-particle wave functions:

$$J \equiv - \int d^3r \phi_i^*(\mathbf{r}) \left( -\frac{\hbar^2}{2m} \nabla^2 + V(\mathbf{r}) \right) \phi_{i+1}(\mathbf{r}), \quad (3.3)$$

$$U_k \equiv \int d^3r \int d^3r' |\phi_i(\mathbf{r})|^2 (g\delta(\mathbf{r} - \mathbf{r}') + V_{\text{dd}}(\mathbf{r} - \mathbf{r}')) |\phi_{i+k}(\mathbf{r}')|^2. \quad (3.4)$$

The index  $i$  is arbitrary, since all wave functions are equal. The on-site energy is explicitly given by

$$U_0 = g \int d^3r |\phi_i(\mathbf{r})|^4 + \int d^3r \int d^3r' |\phi_i(\mathbf{r})|^2 V_{\text{dd}}(\mathbf{r} - \mathbf{r}') |\phi_i(\mathbf{r}')|^2.$$

While  $U_0$  depends on both the dipolar interaction and the contact interaction, the inter-site parameters only depend on the dipolar interaction:

$$U_k = \int d^3r \int d^3r' |\phi_i(\mathbf{r})|^2 V_{\text{dd}}(\mathbf{r} - \mathbf{r}') |\phi_{i+1}(\mathbf{r}')|^2, \quad k \geq 1.$$

---

<sup>3</sup>We have dropped the term  $\sum_i \mu_i \hat{n}_i$  with  $\mu_i = \int d^3r V(\mathbf{r}) |\phi(\mathbf{r})|^2$  since  $\mu_i = \mu$  is constant and the whole sum is only a constant shift  $\mu N_A$  in energy.



For some calculations we will assume that the inter-site interaction energy scales like the (distance)<sup>-3</sup> which is only correct in the limit of large distances<sup>4</sup> as we have seen in section 2.2. We will therefore set  $U_k = \frac{U_1}{k^3}$  for  $k \geq 2$  which leaves us with three free parameters, namely  $J, U_0$  and  $U_1$ .

### Effective Hamiltonian

The sum in the on-site part of the Bose-Hubbard Hamiltonian can be expressed in a slightly different way which will be useful in the following:

$$\begin{aligned} \sum_{i=1}^{N_S} \hat{n}_i (\hat{n}_i - 1) &= \sum_{i=1}^{N_S} \hat{n}_i^2 - N_A = \left( \sum_{i=1}^{N_S} \hat{n}_i \right)^2 - \sum_{i \neq j} \hat{n}_i \hat{n}_j - N_A \\ &= N_A^2 - N_A - 2 \sum_{k=1}^{N_S-1} \sum_{\langle i,j \rangle_k} \hat{n}_i \hat{n}_j. \end{aligned}$$

With this we can reformulate equation (3.2) to

$$\hat{H} = -J \sum_{\langle i,j \rangle} \hat{a}_i^\dagger \hat{a}_j + \frac{1}{2} N_A (N_A - 1) U_0 + \sum_{k=1}^{N_S-1} \left( (U_k - U_0) \sum_{\langle i,j \rangle_k} \hat{n}_i \hat{n}_j \right).$$

The term  $\frac{1}{2} N_A (N_A - 1) U_0$  is a constant shift in energy, independent of the particular state. We can subtract it and define an effective Hamiltonian

$$\hat{H}_{\text{eff}} = -J \sum_{\langle i,j \rangle} \hat{a}_i^\dagger \hat{a}_j + \sum_{k=1}^{N_S-1} \left( (U_k - U_0) \sum_{\langle i,j \rangle_k} \hat{n}_i \hat{n}_j \right). \quad (3.5)$$

Note that there is no on-site interaction part in the effective Hamiltonian. This is instead compensated by a modified inter-site coupling  $U_k \rightarrow U_k - U_0$ .

## 3.2. Double-well system

The simplest multi-well system we can think of is the double-well. Writing down the Hamiltonian

$$\hat{H}_{\text{eff}} = -J (\hat{a}_1^\dagger \hat{a}_2 + \hat{a}_2^\dagger \hat{a}_1) + (U_1 - U_0) \hat{n}_1 \hat{n}_2,$$

we see that the case with inter-site interactions ( $U_1 \neq 0$ ) is not exceptional. We can map it to a purely on-site Hamiltonian by redefining  $U_0 \rightarrow \tilde{U}_0 + U_1$ . The dipolar system certainly behaves differently compared to the purely contact-interacting one but it can be explained by a simple shift in the parameters. There are no new features or effects to be expected from the viewpoint of the Bose-Hubbard model.

<sup>4</sup>The dimensionless distance  $\lambda = l/\sigma_\rho$  has to be much larger than 1 or the distance  $l$  between two wells has to be much larger than the radial size  $\sigma_\rho$  of a single condensate.

### 3.3. Triple-well system

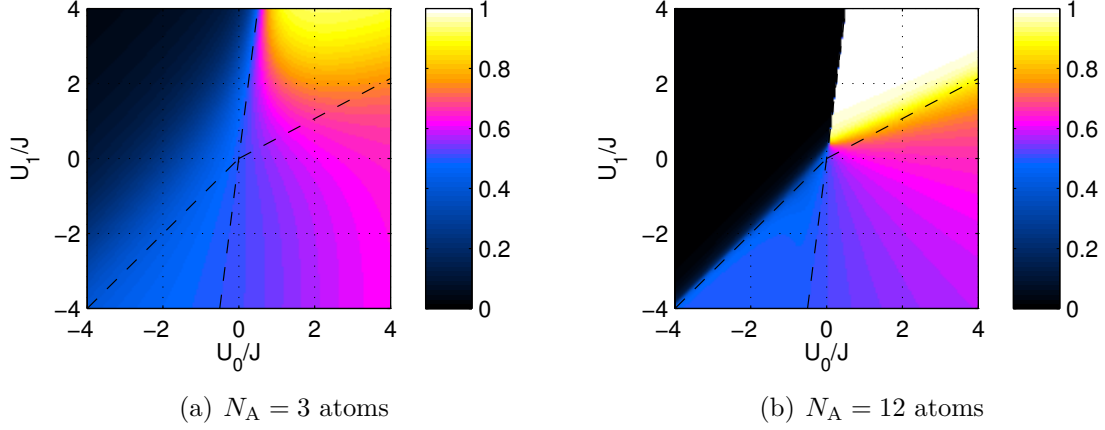


**Figure 3.2.:** Phase diagrams of the triple-well system for different particle numbers. Color indicates the normalized mean number  $\langle \hat{n}_1 + \hat{n}_3 \rangle / N_A$  of atoms in both outer wells. Dashed lines indicate the expected phase boundaries by the variational method (see chapter 4 for details). For a large number of atoms four distinct phases appear.

Our next attempt to see traces of dipolar interactions is the triple-well system. It will turn out to show some non-trivial effects. Its Hamiltonian has the form

$$\hat{H}_{\text{eff}} = -J (\hat{a}_1^\dagger \hat{a}_2 + \hat{a}_2^\dagger \hat{a}_3 + \text{h.c.}) + (U_1 - U_0) \hat{n}_2 (\hat{n}_1 + \hat{n}_3) + (U_2 - U_0) \hat{n}_1 \hat{n}_3.$$

We use exact diagonalization techniques as in [14] to compute the ground state. The resulting “phase diagram” for different particle numbers is shown in figure 3.2. For the computations we use  $U_2 = U_1/2^3$  as described. We will discuss in detail the several phases and states of the triple-well system in section 4.3.2 (see figure 4.3 on page 42 for a visualization).

A precise description of the quantum states for several limiting cases is given in [14]. We do not repeat the discussion here as we will see that most of the states are only accessible for very small atom numbers (when the stability of the single wells is not of relevance, see chapter 6).

### 3.4. More wells: complexity of the problem

For the general multi-well system, the Hilbert space is of dimension

$$\dim(\mathcal{H}) = \binom{N_A + N_S - 1}{N_A} = O(N_A^{N_S-1}),$$

where atom number conservation already reduces the dimensionality. For more than three wells an exact diagonalization for a reasonable number of atoms is computationally out of reach. Typical algorithms for the diagonalization of a  $n \times n$  matrix have a complexity of  $O(n^3)$  which leads to  $O(N_A^{3(N_S-1)})$  for the diagonalization of the  $N_S$ -well Hamiltonian. Even for the triple-well system the complexity is still of order  $O(N_A^6)$  what makes it impractical to treat more than  $N_A \approx 50$  atoms numerically<sup>5</sup>.

In the next chapter we will take another approach, the variational method, which can handle a large number of wells in a reasonable computation time.

---

<sup>5</sup>The phase diagram does not change much for  $N_A > 10$  though.



## 4. Variational method

*When the barriers in the multi-well potential are too large for particles to tunnel through, the system is dominated by the interplay between on-site and inter-site energy. In this regime the ground state of the system is found by minimizing an energy functional which only depends on the occupation numbers. We derive an approximate method which can be used to find ground states for a large number of wells.*

### 4.1. Derivation and approximations

In the  $J = 0$  case the Bose-Hubbard Hamiltonian (3.5) is only a function of the different number operators  $\hat{n}_i$ . Therefore Fock-states  $|n_1, n_2, \dots, n_{N_S}\rangle$  are eigenstates of the system and we can find the ground state by a purely “classical” calculation. We look for the Fock-state with the lowest energy

$$\hat{H}_{\text{eff}} |n_1, n_2, \dots, n_{N_S}\rangle = E |n_1, n_2, \dots, n_{N_S}\rangle,$$

where

$$E = \sum_{k=1}^{N_S-1} \left( (U_k - U_0) \sum_{\langle i,j \rangle_k} n_i n_j \right).$$

Throughout this chapter we will use  $U_k = \frac{U_1}{k^3}$  as described previously. The quantity we are going to minimize is the dimensionless energy  $\tilde{E} \equiv \frac{E}{|U_0|}$  given by

$$\tilde{E} = \sum_{k=1}^{N_S-1} \left( \left( \frac{\nu}{k^3} - \delta \right) \sum_{\langle i,j \rangle_k} n_i n_j \right).$$

Here we have defined the ratio between inter- and on-site energy  $\nu \equiv \frac{U_1}{|U_0|}$  and the sign of the on-site interaction as  $\delta \equiv \frac{U_0}{|U_0|} = \text{sign}(U_0)$ .

The basic assumption in this chapter will be that we can replace the occupation numbers  $n_i \in \mathbb{N}$  by real numbers  $n_i \in \mathbb{R}$ . This is certainly a good approximation if the occupation numbers are much larger than one. One should remember however that we had to assume that the interaction energy  $\propto gN^2$  is small compared to the excitation energy to higher levels when deriving the Bose-Hubbard model. This does not necessarily lead to a contradiction, but the coupling strength  $g$  has to be small. Nevertheless, the

model above is particularly useful as the energy is a quadratic form of the occupation numbers which leads to linear equations in the variational approach. Using a more complex expression<sup>1</sup> would lead to a set of nonlinear equations with no clear strategy how to solve them.

After the replacement by real numbers we can find the *local* minimum of the energy with a variational calculation. We have to add a Lagrange multiplier  $\mu$  to assure that the number of atoms is conserved<sup>2</sup>. The minimization condition is

$$\nabla_n \left[ \tilde{E} - \mu \left( \sum_{i=1}^{N_S-1} n_i - N_A \right) \right] \stackrel{!}{=} 0.$$

This leads to the following set of linear equations for the  $n_i$ :

$$\sum_{k=1}^{N_S-1} \left( \frac{\nu}{k^3} - \delta \right) (n_{i-k} + n_{i+k}) = \mu, \quad \sum_{k=1}^{N_S} n_i = N_A, \quad (4.1)$$

where the numbers  $n_i$  for  $i \notin \{1, \dots, N_S\}$  should be set to zero.

We can do the same for the original Hamiltonian (3.2), resulting in a slightly different set of equations

$$\delta \cdot n_i + \sum_{k=1}^{N_S-1} \frac{\nu}{k^3} (n_{i-k} + n_{i+k}) = \tilde{\mu}, \quad \sum_{k=1}^{N_S} n_i = N_A. \quad (4.2)$$

Both sets of equations (4.1) and (4.2) lead to the same results. A general feature of both is the symmetry<sup>3</sup>

$$(n_1, n_2, \dots, n_{N_S}) \leftrightarrow (n_{N_S}, n_{N_S-1}, \dots, n_1)$$

which is flipping the multi-well along the lattice direction. This has a direct consequence for the solutions which also have to be symmetric under this transformation<sup>4</sup>.

## 4.2. Recursive algorithm to find the ground state

Solving the set of linear equations (4.1) or (4.2) results in a set of occupation numbers  $\{n_i | i = 1, \dots, N_S\}$  which give a *local* extremal value of the energy  $E_v = H(\{n_i\})$ . There are however several conditions to be checked.

---

<sup>1</sup>See chapter 5 for details.

<sup>2</sup>The Lagrange multiplier  $\mu$  is identical with the chemical potential (measured in units of  $|U_0|$ ).

<sup>3</sup>Both sets of equations can be written as  $A\mathbf{n} = \mu$  where  $A = A^t$  is a symmetric matrix.

<sup>4</sup>This is only true if the solution is unique. The determinant of the linear equations though is only zero for special values of the parameters  $\delta, \nu$ . In these cases the solution of equations (4.1), (4.2) is not the real ground state anyway (see section 4.2).

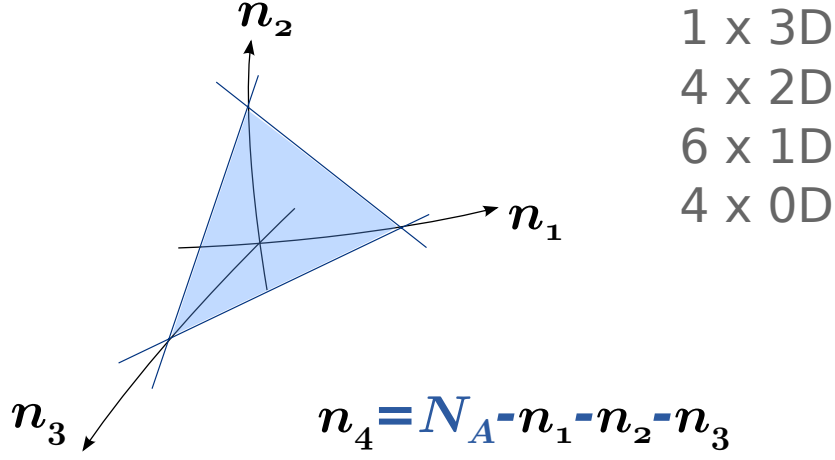


**Figure 4.1.:** For a system with four wells the occupation number space is three-dimensional since the four-dimensional space is restricted by atom number conservation. To find the ground state, the 3D subspace (blue tetrahedron) has to be searched for a global minimum in energy. If the solution of equations (4.1) or (4.2) yields a solution which is not the global minimum or outside the physical space, the boundary subspaces have to be searched. These are four enclosing 2D surfaces, six 1D edges and four 0D points. In general, for the  $N_S$ -well system there are  $\binom{N_S}{k+1}$  subspaces of dimension  $k$  and therefore  $2^{N_S} - 1$  subspaces in total.

First, the solution might be outside the physical range ( $n_i < 0$  or  $n_i > N_A$ ). Second, the energy might be a maximum<sup>5</sup>. And last, the solution might not be the *global* minimum<sup>6</sup>. In all cases, the true ground state has to be located at the *boundary* of the  $(N_S - 1)$ -dimensional occupation number subspace<sup>7</sup>.

A way to tackle this problem is to reduce it recursively in dimensionality. If one of the above conditions applies (and the solution of the set of linear equations is not the real ground state), a single occupation number  $n_i = 0$  is set to zero and the solution in the reduced subspace is calculated. The energies for the different  $i$ 's are compared and the lowest is taken.

Let  $C$  be a set of constraints (site numbers which should be taken to zero). Then we

<sup>5</sup>If the energy is larger than zero, it has to be a maximum as there is always a solution with zero energy ( $n_1 = N_A, n_i = 0$ ).

<sup>6</sup>There is a way to decide *a priori* if the local minimum is the global one. If the matrix describing the set of linear equations is positive-definite the solution has to be the global minimum. Even if some eigenvalues are negative this can still hold if the corresponding eigenvectors violate atom number conservation, like  $(1, 1, 1)^t$  in the triple-well situation.

<sup>7</sup>It is  $N_S - 1$  dimensional since it is restricted by  $\sum_{i=1}^{N_S} n_i = N_A$ .

define the following recursive algorithm<sup>8</sup> to find the ground state and its energy:

$$\tilde{E}_v(C) \equiv \begin{cases} \text{solution of (4.1) or (4.2),} & \text{if solution is the global minimum} \\ & \text{and inside the physical range.} \\ \min_{i \in \{1, \dots, N_S\} \setminus C} E_v(C \cup \{i\}), & \text{otherwise.} \end{cases} \quad (4.3)$$

The ground state and its energy are now found by starting with zero constraints on the atom numbers:  $\tilde{E}_{\text{GS}} = \tilde{E}_v(\{\})$ . An example on how the occupation number space looks like for a small number of wells is shown in figure 4.1.

### 4.3. Exact solution for few wells

The set of linear equations can easily be solved if the number of wells is small. For larger numbers, the conditions for the phase boundaries get more complex and no additional insight is gained. In the following we give the exact solution for two and three wells.

#### 4.3.1. Solution for two wells

The linear equations (4.1) for the double-well are

$$(\nu - \delta)n_2 = \mu \quad (\nu - \delta)n_1 = \mu \quad n_1 + n_2 = N_A,$$

from which we immediately extract the solution  $\mathbf{n} = (n_1 | n_2) = N_A (1/2 | 1/2)$  if it holds that  $\nu \neq \delta \Leftrightarrow U_0 \neq U_1$ . The energy of the double-well is given by  $\tilde{E} = (\nu - \delta)n_1 n_2$ . The solution is thus only a minimum in energy if  $\nu > \delta$ .

In the case  $\nu < \delta$  the lowest energy possible is zero and the solution is either  $(N_A | 0)$  or  $(0 | N_A)$ . In the special case  $\nu = \delta$  every distribution  $(n_1 | n_2)$  has zero energy.

#### 4.3.2. Solution for three wells

For three wells we have the following set of equations

$$\begin{aligned} (\nu - \delta)n_2 + (\nu/8 - \delta)n_3 &= \mu & (\nu - \delta)n_2 + (\nu/8 - \delta)n_1 &= \mu \\ (\nu - \delta)(n_1 + n_3) &= \mu & n_1 + n_2 + n_3 &= N_A \end{aligned}$$

which has the solution

$$\mathbf{n} = N_A \left( \frac{8\delta - 8\nu}{24\delta - 31\nu} \mid \frac{8\delta - 15\nu}{24\delta - 31\nu} \mid \frac{8\delta - 8\nu}{24\delta - 31\nu} \right) \quad (4.4)$$

---

<sup>8</sup>The algorithm terminates in any case if it reaches a one dimensional subspace.



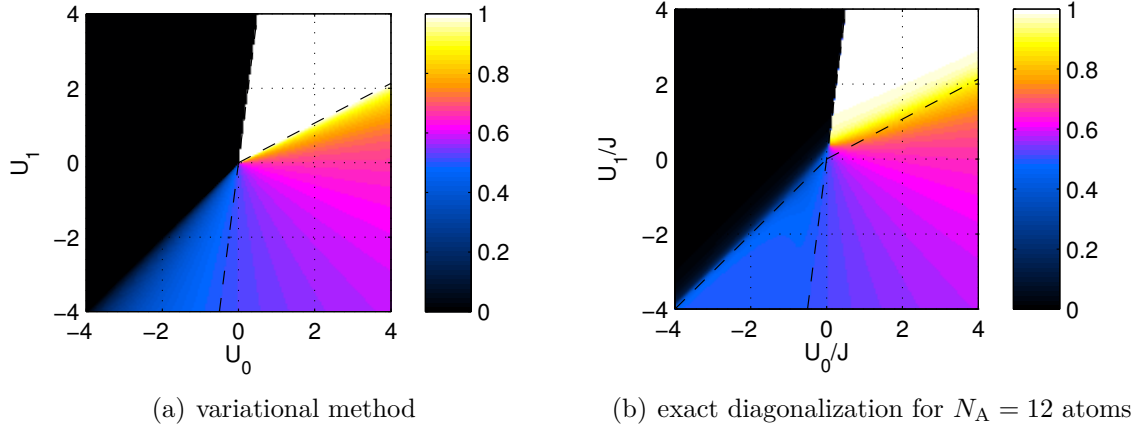


**Figure 4.2.:** (a) Phase diagram of the triple-well system found with the variational method. The color indicates the normalized mean number  $\langle n_1 + n_3 \rangle / N_A$  of atoms in the first plus third well. Dashed lines indicate the expected phase boundaries by the variational method. The diagram contains redundant information as it is only depending on the polar angle (or the ratio  $U_1/U_0$ ). (b) For comparison, phase diagram computed for the Bose-Hubbard model with 12 atoms (cf. figure 3.2). The quantitative agreement is fine and shows that the variational method already works well for a few atoms (away from the center region, i.e. for  $|U_i| > J$ ).

This solution is only physical and a minimum in energy if  $\delta = 1$ ,  $\nu \leq \frac{8}{15}$  or  $\delta = -1$ ,  $\nu < -8$ . For the other regions we find fixed solutions:

$$\mathbf{n} = N_A \cdot \begin{cases} (1/2 | 0 | 1/2), & \delta = 1 \text{ and } \frac{8}{15} < \nu < 8. \\ (1 | 0 | 0) \text{ or } (0 | 1 | 0) \text{ or } (0 | 0 | 1), & (\delta = 1 \text{ and } \nu > 8) \\ & \text{or } (\delta = -1 \text{ and } \nu > -1). \\ (1/2 | 1/2 | 0) \text{ or } (0 | 1/2 | 1/2), & \delta = -1 \text{ and } -8 < \nu < -1. \\ \text{result of (4.4)} & \text{otherwise.} \end{cases} \quad (4.5)$$

The same result can be found in [14, 40]. Figure 4.2 compares the variational method to the exact diagonalization of the Bose-Hubbard Hamiltonian for the triple-well<sup>9</sup>. The quantitative agreement shows that the variational method works well for small  $J$  and  $N_A \gtrsim 10$  atoms.

Especially the states of phase B with the  $(N_A/2 | 0 | N_A/2)$  distribution clearly demonstrate the nonlocal character of the dipolar interactions (see figure 4.3 for a visualization

<sup>9</sup>Note that the mean value in the expression  $\langle n_1 + n_3 \rangle / N_A$  only applies if there are several degenerate states. We did not take the mean value for the black region but rather set this explicitly to zero to compare it to the exact diagonalization. The variational method finds all three states  $(1 | 0 | 0)$ ,  $(0 | 1 | 0)$  and  $(0 | 0 | 1)$  but the second one is favored due to the presence of tunneling in the Bose-Hubbard model.

of the different phases). Due to the strong repulsion, all particles are removed from the middle well and distributed evenly in the outer wells.

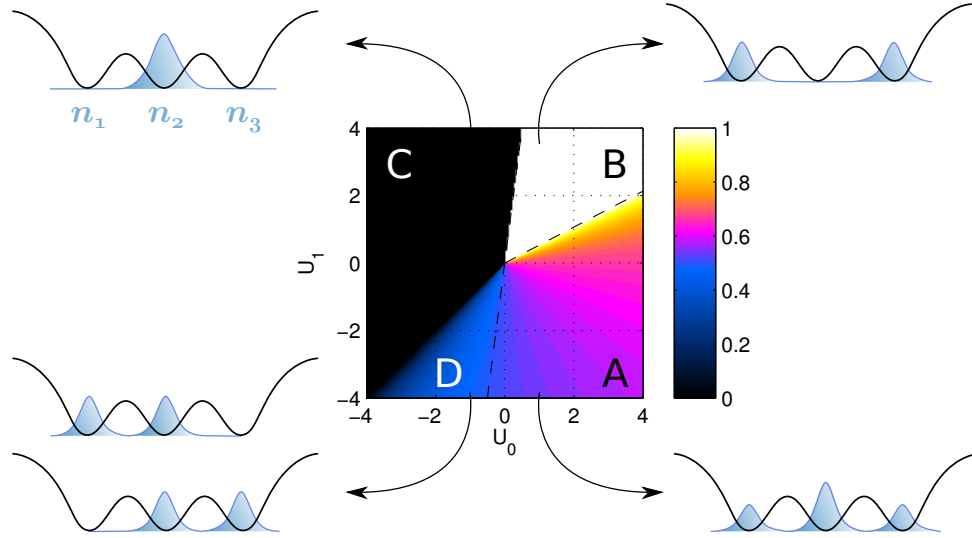


**Figure 4.3.:** Visualization of the four different phases in the triple-well system. **Phase A** is the only region with a real dependence on the interaction ratio  $\frac{U_1}{U_0}$ . The state is given by equation (4.4). For  $U_1 < 0$  we have  $n_2 > n_1, n_3$  whereas the inverse is true for  $U_1 > 0$ . For zero dipolar interaction all wells are equally populated. **Phase B** is characterized by a strong dipolar repulsion and has no particles in the middle well. **Phase C** is dominated by the on-site energy which attracts all particles to one well (see comment in figure 4.2 on the degeneracy in this region). **Phase D** finally is a result of a strong attractive inter-site coupling and has no particles in either the left or right well.

## 4.4. General features of the multi-well states

The states found by the variational method and the recursive algorithm (4.3) show some features which hold in general for a large number of sites  $N_S$ . For  $\nu = \frac{U_1}{|U_0|} = 0$  we can immediately deduce the ground state which has all sites equally occupied (see figure 4.4 for an example with 11 wells).

**Attractive inter-site interaction:** For  $\nu < 0$  the wells in the middle of the structure get more and more populated until the outer sites are completely empty. For very large  $|\nu|$  we find that only three sites are occupied (see figure 4.4(a)). The state is the same as in the triple-well situation<sup>10</sup> as described by equation (4.4) in the limit  $\nu \gg \delta$ . There are

<sup>10</sup>The triplet may be moved to every site in the lattice without energy change, so there are  $N_S - 2$  degenerate states.

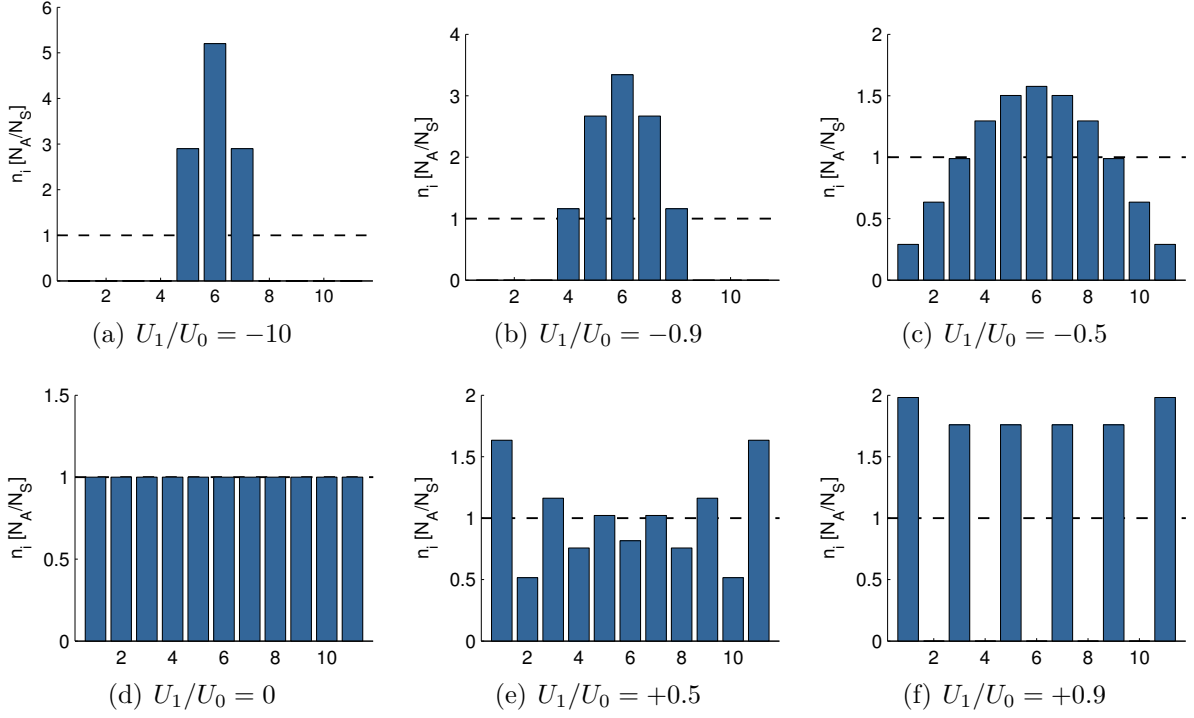


**Figure 4.4.:** States in the 11-well system, calculated with the variational method and the recursive algorithm (4.3). For all states  $U_0 > 0$ . The dashed line shows the occupation level for equally occupied sites ( $N_A/N_S$ ). For attractive interaction (first row) the particles quench together in the middle of the structure. For very large attraction only three sites are occupied. Repulsive interaction (last two figures) leads to a structure formation where every second lattice site is empty.

$\frac{8}{31}N_A$  atoms at both sides and  $\frac{15}{31}N_A$  atoms in the middle:

$$\left(0 \left| \dots \left| 0 \left| \frac{8}{31}N_A \left| \frac{15}{31}N_A \left| \frac{8}{31}N_A \left| 0 \left| \dots \left| 0 \right.\right.\right.\right.\right.\right.\right.$$

**Repulsive inter-site interaction:** For  $\nu > 0$  we observe oscillations with a period of two lattice sites. For strong repulsive interactions every second lattice site is empty. Even larger interaction energies lead to a movement of the particles to both borders (finite size effect, as the outer wells have no neighbors, cf. 4.4(f)).

#### 4.4.1. Dependence on the cut-off parameter

The ground states which are computed with the variational method include all inter-site interactions (nearest neighbor, second nearest neighbor, ...). If the interaction is artificially cut-off at some distance, the density profile changes significantly as shown in figure 4.5. The difference is still visible for a seemingly large cut-off of 3, when only the interactions starting from the fourth-nearest neighbor are neglected (which has only  $U_4/U_1 = 4^{-3} = 1,6\%$  of the strength of the  $U_1$  term). This explicitly demonstrates how important it is to keep all interaction terms.

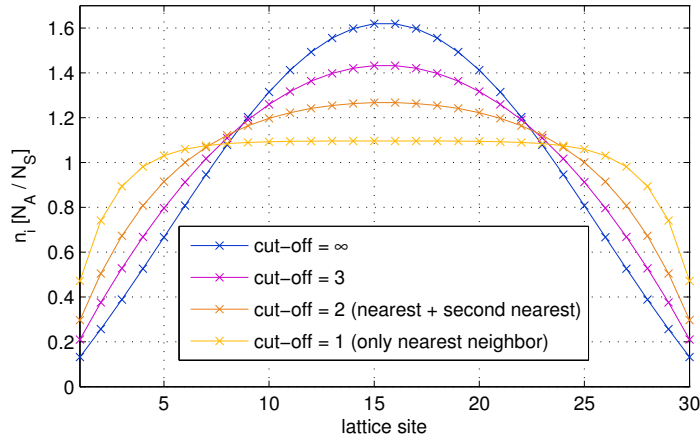


**Figure 4.5.:** Density profile (occupation numbers for the individual lattice sites) for a 30-well system with and without cut-off of the dipolar interaction. The cut-off defines at which distance the inter-site interaction is neglected and set to zero. A cut-off of 2 means that nearest and second-nearest neighbors (4 sites) are taken into account. Only for a large cut-off value the profile approaches the true ground state (blue, no cut-off). The interaction ratio is  $\nu = \frac{U_1}{|U_0|} = -0.43$  and  $U_0 > 0$ .

## 5. Scaling of the interaction energy

*We have used the Bose-Hubbard model to describe the physics of multi-well potentials. One of the main quantities is the on-site interaction energy which has a fixed quadratic scaling with the number of particles in each well.*

*In this chapter the calculation of this parameter is analyzed with particular respect to the number of particles. We show that the interaction energy exhibits a different scaling behavior, depending on the dimensionality. Therefore the Bose-Hubbard energy term is only a good approximation in the regime of low filling rates.*

*Only contact-interacting condensates are considered in this section. We investigate the general case of  $d$  dimensions in a harmonic trap with different methods. For the analytic calculations we work in two different regimes. In the weakly interacting case we use a Gaussian ansatz. Additionally, the strongly interacting case is investigated in the Thomas-Fermi regime. We compare both analytical calculations to numerical simulations and show that all methods predict the same scaling with the number of particles.*

### 5.1. On-site interaction energy

Once the wave function in one well is known, the on-site interaction energy can be calculated<sup>1</sup> as shown in equation (1.9):

$$E_{\text{on-site}} = \frac{N^2}{2} \cdot g^{(d)} \int d^d r |\Psi(\mathbf{r})|^4 = \frac{N^2}{2} \cdot U_0, \quad (5.1)$$

where  $g^{(d)}$  is the coupling strength in  $d$  dimensions (in 3D we have  $g^{(3)} = 4\pi\hbar^2 a/m$  as before<sup>2</sup>) and  $N$  is the number of particles (in one well).

Although  $\Psi$  is normalized to unity, the Bose-Hubbard parameter  $U_0 = g^{(d)} \int d^d r |\Psi(\mathbf{r})|^4$  as defined in equation (3.4) is still depending on  $N$  since the shape of the wave function is changing with the number of particles (growing interaction energy for larger  $N$  if  $g > 0$ ).

In the following  $E_{\text{on-site}}(N)$  is calculated with different methods. We show that the scaling behavior is universal for all of them.

---

<sup>1</sup>Note that we still use  $\frac{N^2}{2}$  instead of the correct expression  $\frac{N(N-1)}{2}$  for the number of interacting particles. If the number of atoms is large the first term is a good approximation as mentioned in chapter 1.3

<sup>2</sup>In 2D, for example, the coupling strength for  $a \ll a_{\text{HO}}$  is  $g^{(2)} = \frac{\sqrt{8\pi}\hbar^2}{m} \frac{a}{a_{\text{HO}}}$  where  $a_{\text{HO}}$  is the harmonic oscillator length in the strongly confining third direction [41, section 6.2].

## 5.2. Gaussian trial function

The idea is to take a Gaussian ansatz (which is exact in the non-interacting case) and use the variational principle to adjust the widths of the different  $\sigma_i$ . The normalized wave function in  $d$  dimensions is

$$\Psi(x_1, \dots, x_d) = \frac{1}{\pi^{\frac{d}{4}} \prod_{i=1}^d \sqrt{\sigma_i}} \exp\left(-\frac{1}{2} \sum_{i=1}^d \frac{x_i^2}{\sigma_i^2}\right).$$

Plugging this into the energy functional of the Gross-Pitaevskii equation for a harmonic external potential (1.9)

$$\frac{E}{N} = \int d^d r \Psi^*(\mathbf{r}) \left( -\frac{\hbar^2}{2m} \nabla^2 + \frac{m}{2} \sum_{i=1}^d \omega_i^2 x_i^2 + \frac{g^{(d)}}{2} N |\Psi(\mathbf{r})|^2 \right) \Psi(\mathbf{r})$$

yields the following energy per particle:

$$\epsilon \equiv \frac{E}{N} = \frac{\hbar^2}{2m} \sum_{i=1}^d \frac{1}{2\sigma_i^2} + \frac{m}{2} \sum_{i=1}^d \frac{\omega_i^2 \sigma_i^2}{2} + \frac{g^{(d)} N}{2(2\pi)^{\frac{d}{2}} \prod_{i=1}^d \sigma_i}.$$

The variational equations read

$$\frac{\partial \epsilon}{\partial \sigma_k} = -\frac{\hbar^2}{2m} \frac{1}{\sigma_k^3} + \frac{m}{2} \omega_k^2 \sigma_k - \frac{g^{(d)} N}{2(2\pi)^{\frac{d}{2}} \sigma_k \prod_{i=1}^d \sigma_i} \stackrel{!}{=} 0.$$

Multiplying by  $2m/\hbar^2 \sigma_k^3$  and rearranging gives:

$$1 = \left( \frac{\sigma_k}{l_k} \right)^4 - \frac{g^{(d)} N m}{(2\pi)^{\frac{d}{2}} \hbar^2 \prod_{i \neq k} \sigma_i}, \quad (5.2)$$

where  $l_k = \sqrt{\hbar/(m\omega_k)}$  is the harmonic oscillator length corresponding to  $\omega_k$ .

From the set of  $d$  equations (5.2) the different  $\sigma_i$  and therefore the minimum energy (and  $U_0$ ) can be calculated.

**No interaction:** For the non-interacting case where the coupling strength  $g^{(d)} = 0$ , we see that the harmonic oscillator solution is recovered as  $\sigma_k = l_k$ .

**Isotropic case:** We are interested in the scaling behavior for large number of atoms<sup>3</sup>. In the  $d$ -dimensional isotropic case ( $\omega_i = \omega$ ,  $\sigma_i = \sigma$ ) the scaling can be extracted from the variational equations. First we rewrite (5.2)

$$1 = u^4 - \tilde{g}^{(d)} \cdot u^{2-d}, \quad (5.3)$$

---

<sup>3</sup>It should be noted that the Gaussian ansatz is an especially good approximation for the *weakly* interacting system. We treat the strongly-interacting case in the next section.

using the dimensionless  $u \equiv \sigma/l$  and the dimensionless coupling

$$\tilde{g}^{(d)} \equiv \frac{g^{(d)} N m}{(2\pi)^{\frac{d}{2}} \hbar^2} \cdot l^{2-d}.$$

For large  $\tilde{g}^{(d)} \gg 1$  the approximate solution<sup>4</sup> of the polynomial equation (5.3) is

$$u \approx \left( \tilde{g}^{(d)} \right)^{\frac{1}{2+d}}.$$

This results in the following scaling relation for the energy in  $d$  dimensions:

$$E_{\text{on-site}}^{(d)} \propto N^2 \cdot \sigma^{-d} \propto N^{2-\frac{d}{2+d}} \propto N^{\frac{4+d}{2+d}}. \quad (5.4)$$

Therefore we have the following scaling exponents: 2 (0D),  $5/3$  (1D),  $3/2$  (2D) and  $7/5$  (3D). Only for zero dimensions the  $U_0$  parameter is constant ( $E_{\text{on-site}}^{(0)} \propto N^2$ ) as assumed in the Bose-Hubbard model.

### 5.2.1. Dimensional crossover

The scaling behavior (5.4) in the Gaussian case was calculated for an isotropic trap. If we reduce one spatial dimension (say,  $z$ ) by enlarging the trapping frequency, there should be a crossover from the  $N^{7/5}$  scaling in the three dimensional case to the  $N^{3/2}$  scaling in the 2D case. In contrast, if the trapping frequency is lowered, the trap gets elongated in one direction and the system should behave more 1D like with a scaling of  $N^{5/3}$ . Figure 5.1 shows the calculated scaling exponent  $\alpha$  in the relation  $E_{\text{on-site}} \propto N^\alpha$  during the crossover from 1D  $\rightarrow$  3D  $\rightarrow$  2D. As expected,  $\alpha$  converges to the predicted values in 1D (2D) for very small (large) trap aspect ratios  $\omega_z/\omega_\rho$ .

## 5.3. Thomas-Fermi regime

As we demonstrated in section 1.3.4, neglecting the kinetic energy term in the Gross-Pitaevskii equation (1.5) turns it to a simple algebraic equation with the solution<sup>5</sup>

$$n(\mathbf{r}) = \frac{1}{g^{(d)}} \left( \mu - \sum_{i=1}^d \omega_i^2 x_i^2 \right) = \frac{\mu}{g^{(d)}} \left( 1 - \sum_{i=1}^d \frac{x_i^2}{R_i^2} \right).$$

The  $R_i$  introduced here are the different Thomas-Fermi radii

$$R_i = \sqrt{\frac{2\mu}{m\omega_i^2}}.$$

<sup>4</sup>This is the solution which is real and positive  $u \in \mathbb{R}^+$

<sup>5</sup>Each inverted parabola has to be cut off at  $R_i$  since the density would be negative otherwise.

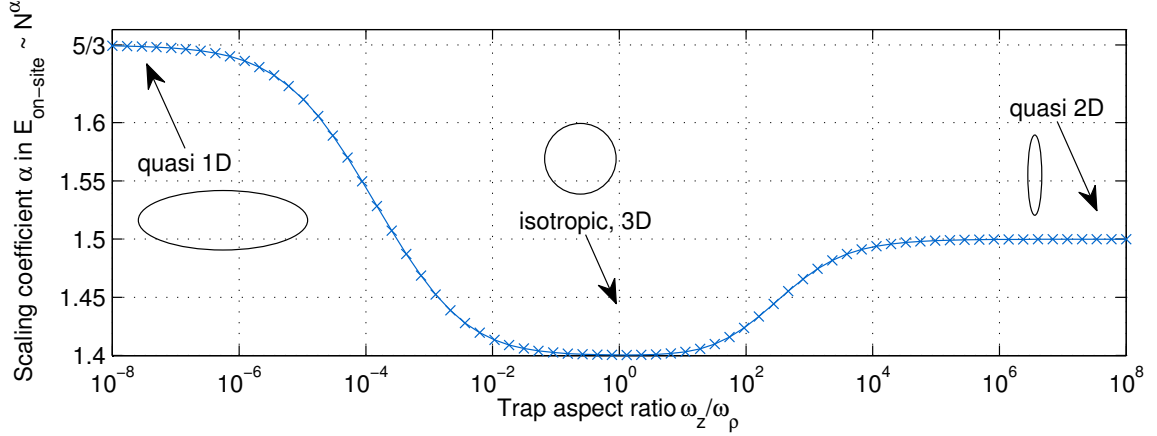


**Figure 5.1.:** Scaling exponent  $\alpha$  in the relation  $E_{\text{on-site}} \propto N^\alpha$  for different trap aspect ratios, calculated with the Gaussian variational method. For 3D the expected scaling is  $\alpha = 7/5 = 1.4$ , for 2D it is  $\alpha = 3/2 = 1.5$  and for 1D  $\alpha = 5/3$ . The exponent increases smoothly between the expected values as the trap is either compressed or expanded in one direction. Starting from an isotropic 3D trap at  $\omega_z/\omega_\rho = 1$  the trap gets more 2D like if the ratio is increased (compression in  $z$ -direction) and more 1D like if the ratio is decreased (decompression in  $z$ -direction).

The on-site energy is calculated as before in equation (5.1):

$$E_{\text{on-site}} = \frac{1}{2} g^{(d)} \int d^d r n(\mathbf{r})^2.$$

We can conclude what the integral yields by looking at the physical dimension:

$$\begin{aligned} \int d^d r n(\mathbf{r})^2 &= \left( \frac{\mu}{g^{(d)}} \right)^2 \int d^d r \left( 1 - \sum_{i=1}^d \frac{x_i^2}{R_i^2} \right)^2 \\ &= \left( \frac{\mu}{g^{(d)}} \right)^2 \prod_{i=1}^d R_i \times \text{numerical factors}. \end{aligned} \quad (5.5)$$

The numerical factors indicated here are depending on the dimensionality but nothing else. The normalization condition

$$N = \int d^d r n(\mathbf{r}) = \frac{\mu}{g^{(d)}} \prod_{i=1}^d R_i \times \text{numerical factors}$$

shows that

$$\prod_{i=1}^d R_i \propto \frac{g^{(d)} N}{\mu}. \quad (5.6)$$



As each radius  $R_i$  is proportional to  $\mu^{\frac{1}{2}}$ , the product  $\prod_{i=1}^d R_i$  is proportional to  $\mu^{\frac{d}{2}}$  and therefore we get (dropping  $g^{(d)}$ , as it is not depending on  $N$ )

$$\mu^{\frac{d}{2}+1} \propto N \iff \mu \propto N^{\frac{2}{2+d}}. \quad (5.7)$$

Combining equation (5.5) with (5.6) gives

$$E_{\text{on-site}} \propto \mu N$$

and thus, including (5.7)

$$E_{\text{on-site}} \propto \mu N \propto N^{\frac{2}{2+d}+1} \propto N^{\frac{4+d}{2+d}}$$

which is exactly the same scaling as in the Gaussian case. Note that we did not assume that the trap is isotropic which means that the Thomas-Fermi calculation suggests no change in the scaling for asymmetric traps. For the behavior in the Gaussian case, see figure 5.1.

## 5.4. Comparison to the numerical solution

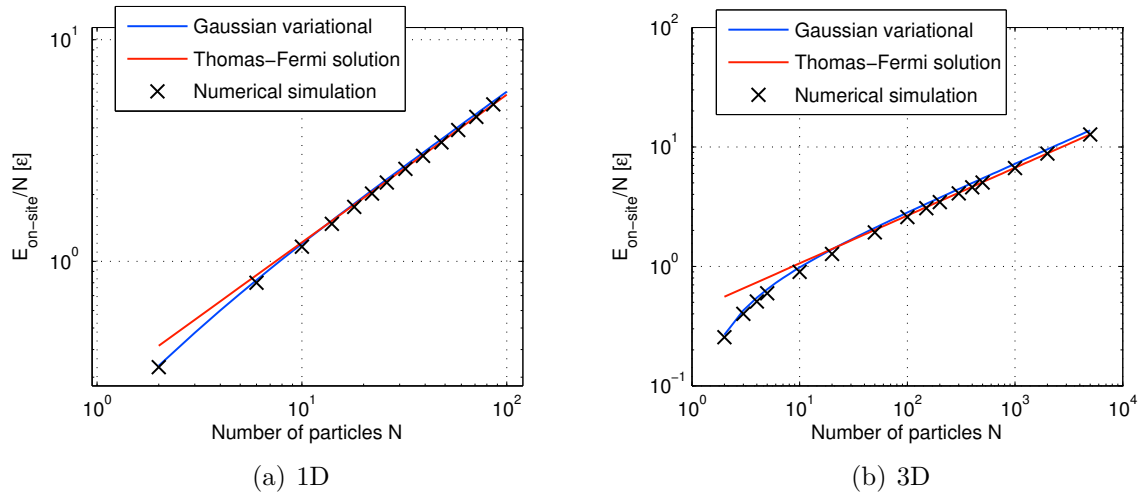


**Figure 5.2.:** Calculations of the on-site energy per particle with different methods in both 1D and 3D. The first method is the variational principle with a Gaussian ansatz, the second an analytical calculation in the Thomas-Fermi regime and last the numerical simulations with imaginary time evolution. All three methods show the same scaling relation for large  $N$  and agree also quantitatively. The Gaussian ansatz works best for a small number of atoms whereas the Thomas Fermi solution fits slightly better to the numerical simulations for large atom numbers.

## 5. Scaling of the interaction energy

---

In 1D and 3D we performed numerical simulations using the method of imaginary time evolution (see chapter 6 for details). As figure 5.2 shows, all three methods (Gaussian ansatz, exact solution in Thomas-Fermi regime and numerical simulations) exhibit the same scaling relation in both 1D and 3D.

Using the numerical simulations as the best reference, we see that the Gaussian ansatz is especially good for a small number of atoms (weak interaction) whereas the Thomas Fermi solution fits best to the numerical simulations for large atom numbers<sup>6</sup>.

---

<sup>6</sup>For all calculations we have used  $a = a_{\text{HO}}$ . Changing the scattering length simply scales the curve linearly (abscissa).

## 6. Numerical simulations

*To support and extend our analytical findings we have performed numerical simulations to compute the ground state of the dipolar Gross-Pitaevskii equation. We solve the integro-differential equation on a 3D grid using the method of imaginary time evolution and the split-step method. The real time evolution is also accessible. We briefly describe the involved methods and present the results of the simulations.*

*For the triple-well situation we compare our numerical results to the states found by the diagonalization of the Bose-Hubbard model and the variational method.*

### 6.1. Methods

#### 6.1.1. Imaginary time evolution

To find the ground state of the system described by the Gross-Pitaevskii equation (1.10) we use the imaginary time evolution method [42]. The basic idea is to replace the time  $t$  by the imaginary parameter  $\tau = -it$ . For small time steps the evolution of the wave function can be written as

$$\Psi(t + \Delta t) = \exp\left(-\frac{i}{\hbar} \hat{H} \Delta t\right) \Psi(t).$$

Inserting  $\tau$  we get

$$\Psi(\tau + \Delta\tau) = \exp\left(-\frac{1}{\hbar} \hat{H} \Delta\tau\right) \Psi(\tau), \quad (6.1)$$

where  $\Psi(\tau + \Delta\tau)$  is not a normalized wave function anymore<sup>1</sup>.

If we assume for simplicity that the ground state energy is zero and decompose the (arbitrary) wave function  $\Psi = \Psi_{\text{GS}} + \delta\Psi$  into ground state and excited parts<sup>2</sup> we get

$$\Psi(\tau + \Delta\tau) = \Psi_{\text{GS}} + \exp\left(-\frac{1}{\hbar} \hat{H} \Delta\tau\right) \delta\Psi(\tau).$$

The second part describes an exponential decay for the excited modes as only eigenvectors with positive eigenvalues (and negative exponent) are left. After a number of successive

---

<sup>1</sup>Typically the wave function is normalized after each evolution step to guarantee numerical stability.

<sup>2</sup>This part is crucial. For the non-linear Gross-Pitaevskii equation a linear decomposition like this is not appropriate. To our knowledge no rigorous proof has been given that the method works for non-linear equations.

evolution steps like in (6.1), the wave function  $\Psi$  which is typically renormalized after each evolution step eventually converges to the ground state wave function  $\Psi_{\text{GS}}$ . In section 6.2.1 we discuss how to decide when the simulation can be stopped.

### 6.1.2. Split-step method

As we have seen, one has to perform evolution steps like the following to simulate the Gross-Pitaevskii equation either in real or imaginary time

$$\Psi' = \exp(\gamma \hat{H} \Delta t) \Psi \quad (6.2)$$

with  $\gamma$  being a coefficient which is either  $-i/\hbar$  (for real-time) or  $-1/\hbar$  (for imaginary-time evolution). The Hamilton operator can be decomposed into several parts describing the *kinetic* energy, the *external* potential, the *contact* interaction and the *dipolar* interaction, respectively:

$$\hat{H} = \hat{H}_{\text{kin}} + \hat{H}_{\text{ext}} + \hat{H}_{\text{con}} + \hat{H}_{\text{dip}}.$$

It is useful to decompose the evolution step in a similar way as the different parts can be calculated in distinct ways. The evolution due to the kinetic part, for example, can be performed efficiently in Fourier space.

As the kinetic energy part does not commute with the other parts of the Hamiltonian<sup>3</sup>, we cannot decompose the exponential of the sum into a product of exponentials. Utilizing the Baker-Campbell-Hausdorff formula<sup>4</sup>

$$e^{(X+Y)\Delta t} = e^{X\Delta t} \cdot e^{Y\Delta t} \cdot e^{-\frac{1}{2}[X,Y]\Delta t^2} \quad (6.3)$$

we see however that we can neglect higher order terms for small  $\Delta t$  and thus use the decomposition as intended:

$$e^{c\hat{H}\Delta t} \approx e^{c\hat{H}_{\text{kin}}\Delta t} \cdot e^{c\hat{H}_{\text{ext}}\Delta t} \cdot e^{c\hat{H}_{\text{con}}\Delta t} \cdot e^{c\hat{H}_{\text{dip}}\Delta t}.$$

The condition that  $\Delta t$  be small can roughly be stated in the following way ( $|\gamma| = 1/\hbar$ ):

$$\max_i |\gamma E_i \Delta t| \ll 1 \quad \Longleftrightarrow \quad \Delta t \ll \frac{\hbar}{\max_i |E_i|}, \quad (6.4)$$

where we have denoted the energies corresponding to the different parts of the Hamiltonian by  $E_i$ . When performing the simulations, (6.4) should be fulfilled to provide numerical stability.

---

<sup>3</sup>The kinetic energy is diagonal in momentum space, the other parts are diagonal in position space.

<sup>4</sup>This version of the BCH formula is only valid if  $[X, [X, Y]] = 0$ , but the lowest order approximation is enough to support the argument.

In the following paragraphs we will discuss the four evolution steps<sup>5</sup> to get from  $\Psi$  to  $\Psi'$  as in equation (6.2):

$$\Psi \xrightarrow{\hat{H}_{\text{con}}} \Psi_1 \xrightarrow{\hat{H}_{\text{dip}}} \Psi_2 \xrightarrow{\hat{H}_{\text{kin}}} \Psi_3 \xrightarrow{\hat{H}_{\text{ext}}} \Psi'.$$

### Evolution due to contact interaction

The contact interaction part is easily performed in real space by multiplying with the exponential factor:

$$\Psi_1 = \exp\left(\gamma \cdot gN |\Psi(\mathbf{r})|^2 \cdot \Delta t\right) \Psi.$$

### Evolution due to dipolar interaction

As shown in section 1.4.2, the dipolar part of the Hamiltonian

$$\hat{H}_{\text{dip}} = \Phi_{\text{dd}}(\mathbf{r})$$

can be calculated in Fourier space as a simple product

$$\mathcal{F}\{\Phi_{\text{dd}}\} = \mathcal{F}\{V_{\text{dd}} \star n\} = (2\pi)^{3/2} \cdot \mathcal{F}\{V_{\text{dd}}\} \cdot \mathcal{F}\{n\}.$$

The evolution step is thus done by

$$\begin{aligned} \Psi_2 &= \exp\left(\gamma \cdot \mathcal{F}^{-1}\left\{(2\pi)^{3/2} \cdot \mathcal{F}\{V_{\text{dd}}\} \cdot \mathcal{F}\{n\}\right\} \Delta t\right) \Psi_1 \\ &= \exp\left(-\gamma \cdot g_{\text{dd}} N \mathcal{F}^{-1}\left\{(1 - 3 \cos^2(\alpha)) \cdot \mathcal{F}\{|\Psi_1|^2\}\right\} \Delta t\right) \Psi_1. \end{aligned}$$

### Evolution due to kinetic energy

The kinetic energy term is diagonal in momentum space

$$\mathcal{F}\left\{-\frac{\hbar^2}{2m} \nabla^2 \Psi(\mathbf{r})\right\} = \frac{\hbar^2 k^2}{2m} \Psi(\mathbf{k})$$

which means that the whole evolution step can be performed in  $k$ -space:

$$\Psi_3 = e^{\gamma \cdot \hat{H}_{\text{kin}} \Delta t} \Psi_2 = \mathcal{F}^{-1}\left\{\exp\left(\gamma \cdot \frac{\hbar^2 k^2}{2m} \cdot \Delta t\right) \mathcal{F}\{\Psi_2\}\right\}.$$

The latter can be seen by expanding the exponential into a series and Fourier transforming each term individually.

<sup>5</sup>The particular order is not of relevance if we neglect the exponentials with  $\Delta t^2$  as can be seen from equation (6.3). The presented sequence has some advantages in memory and CPU usage.

### Evolution due to the external potential

The part for the external potential is also done in real space

$$\Psi' = \exp(\gamma \cdot V(\mathbf{r}) \cdot \Delta t) \Psi_3.$$

## 6.2. Preparations

### 6.2.1. Verification of the results

Performing numerical simulations with the imaginary time evolution method requires certain checks for the reliability of the final result. The easiest test is the convergence of the total energy. This however does not guarantee that the simulation has converged to the ground state. The following method can be used to check if the final state is close to the ground state. In the presented way it only works for power-law potentials  $V(\mathbf{r}) \propto \mathbf{r}^n$  such as the (spherical) harmonic potential.

**Virial expression:** Suppose that a given wave function  $\Psi(\mathbf{r})$  is the ground state of the Hamiltonian  $\hat{H}$ . Then scaling the wave function<sup>6</sup>  $\Psi_\alpha(\mathbf{r}) = \alpha^{3/2} \Psi(\alpha \mathbf{r})$  by a factor  $\alpha$  must lead to a state with higher energy. Therefore it has to hold that

$$\left. \frac{\partial}{\partial \alpha} \langle \Psi_\alpha | \hat{H} | \Psi_\alpha \rangle \right|_{\alpha=1} \stackrel{!}{=} 0.$$

Expressing the left side in terms of the different energy contributions of the *initial* state  $\Psi(\mathbf{r})$  leads to the condition

$$V \equiv 2E_{\text{kin}} - nE_{\text{pot}} + 3(E_{\text{con}} + E_{\text{dip}}) = 0$$

which is known as the virial theorem ( $n$  is the exponent in the power law  $\mathbf{r}^n$ ).

Figure 6.1(a) shows the total energy and the virial expression  $V$  during a simulation in a spherical harmonic trap ( $n = 2$ ). Both quantities converge exponentially. The virial reaches some finite value which is caused mainly by a finite time step  $\Delta t$  as shown in figure 6.1(b).

### 6.2.2. Procedure for a multi-well simulation

The following sequence is used to guarantee that our numerical procedure to find the ground state for the dipolar multi-well situation is working properly.

**step 1:** The simulation is set up with an initial Gaussian wave function which spreads over all wells<sup>7</sup>. There are less atoms in the outer wells with this definition but

---

<sup>6</sup>This wave function is normalized since  $\int d^3r \Psi_\alpha(\mathbf{r}) = \int d^3(\alpha \mathbf{r}) \Psi(\alpha \mathbf{r}) = 1$ .

<sup>7</sup>Usually the spreading is such that  $\sigma$  in lattice direction is half the size of the grid.

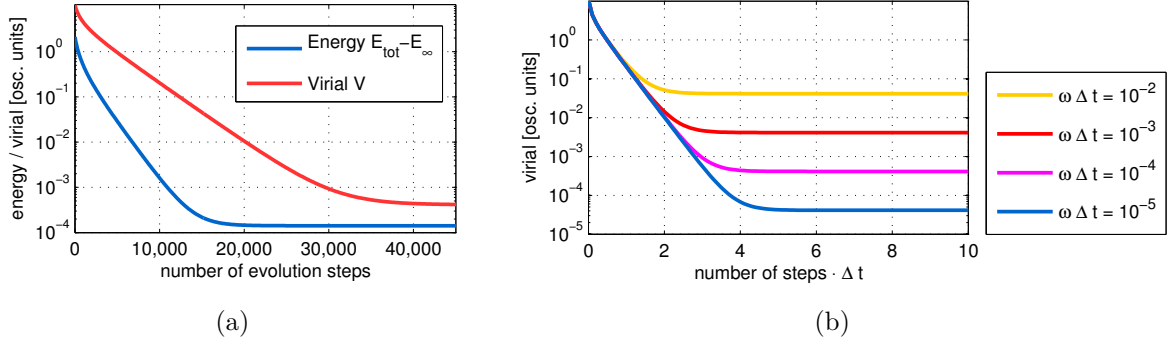


**Figure 6.1.:** (a) Logarithmic plot of the total energy (with subtracted offset found by an exponential fit) and the virial  $2(E_{\text{kin}} - E_{\text{pot}}) + 3E_{\text{con}}$  monitored during an imaginary time evolution for a spherical harmonic trap with  $a \cdot N/a_{\text{HO}} = 10$ , no dipolar interaction and a time step of  $\Delta t = 0.0001\omega^{-1}$ . Both quantities converge exponentially and the virial goes to zero, as expected. The final offset is due to numerical errors (finite  $\Delta t$ ). The virial is converging slower than the total energy which means that the distribution of energies (and the wave function) is still changing after the energy already converged to the final value (after  $\approx 20,000$  steps). (b) Virial for the same simulation, monitored for different time steps  $\Delta t$ . The offset virial decreases with smaller time steps, as expected. More evolution steps are needed, though (axis is scaled by  $\Delta t$  for the different curves).

we check in the end (step 5) that the tunneling is large enough<sup>8</sup> to find the true ground state.

**step 2:** All interactions are “switched off” (no evolution due to contact or dipolar interaction), the ground state for the *non-interacting* case is found by imaginary time evolution.

**step 3:** The contact interaction is switched on<sup>9</sup>, the ground state for the purely *contact interacting* case is found by subsequent imaginary time evolution (starting from the non-interacting case). We do not yet switch on the dipolar interaction in this step since the time evolution otherwise is likely to cross instability regions (see section 1.4.1 for details).

**step 4:** The dipolar interaction is now switched on and again the ground state is reached, now for the full *contact and dipolar interacting* case.

<sup>8</sup>If the tunneling rate between the different wells is too low, the imaginary time evolution takes an exponentially long time to find the real ground state.

<sup>9</sup>Steps 3 and 4 are interchanged if the scattering length is negative. For the diagrams of figures 6.4 and 6.6 we use a slightly different scheme where we start at high scattering lengths and scan a complete line by lowering  $a$  until the state collapses.

**step 5:** Both interaction types are switched off again, the ground state for the non-interacting case should now be reached again. If the tunneling is too low, the state will now be different from the one in step 1.

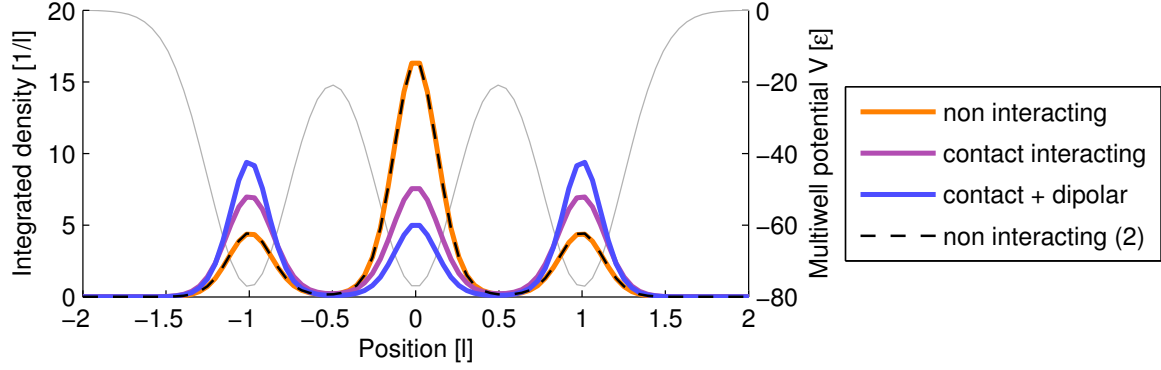


**Figure 6.2.:** Density (integrated in both directions perpendicular to the lattice) for a sample triple-well simulation (repulsive inter-site). The orange line shows the ground state of the non-interacting situation (step 2 in the text). The purple line is the ground state of the purely contact interacting case (step 3) and the blue line finally shows the fully interacting state (step 4). The dashed line indicates the second non-interacting state (step 5). Outlined in gray is the external Gaussian multi-well potential.

## 6.3. Triple-well simulations

Our main motivation to simulate the Gross-Pitaevskii equation for the triple-well situation is to support our findings from the Bose-Hubbard model and the variational approach. In particular, we are interested in the states which clearly demonstrate the inter-site effects like phase B with the  $(N/2 | 0 | N/2)$  states.

### 6.3.1. Geometrical considerations

Performing the triple-well simulations, we have to choose a certain geometry and different parameters of the external multi-well potential (introduced in section 2.1), like the spacing between two wells  $l$ , the widths of a single well in all spacial directions  $w_x, w_y, w_z$  and the depth of the potential  $V_0$ .

The parameter space is too large to scan it completely (in the end we only want to change the interaction parameters  $a, a_{dd}, N$  and the polarization direction). We reduce it by choosing reasonable values for the parameters, having symmetries as well as physical and experimental limitations in mind (for a detailed comparison to the experimentally accessible regions, see appendix A).



**The spacing:** We use the spacing  $l$  between two wells as the unit of length (see section 1.3.3). Therefore we do not have to choose a certain value for it. The other dimensionless parameters depend on  $l$ , however (see appendix A.2).

**The widths:** If  $z$  is the direction of the triple-well potential, the width  $w_z$  in this direction is also restricted. For  $w_z \gg 0.5l$  the different wells are not clearly distinct whereas for  $w_z \ll 0.5l$  the tunneling is too low to find the ground state of the system with either imaginary time evolution or in an experiment<sup>10</sup>. In the present simulations we will therefore keep  $w_z = 0.5l$ .

To find values for  $w_x$  and  $w_y$ , we ask for two conditions on our external potential:

1. As we focus especially on inter-site effects, changing the polarization direction (from an attractive inter-site coupling to a repulsive one) should not change the *on-site* energy<sup>11</sup>.
2. The stability of a single well should be higher than in the spherical case (lower  $a_{\text{crit}}$  for the same  $a_{\text{dd}}$ ).

To satisfy the first condition, the width in one of the directions perpendicular to  $z$  has to be equal to  $w_z$ . Without loss of generality we define  $x$  to be the polarization direction for the “repulsive geometry” ( $z$  for the “attractive” case). Therefore we have  $w_x = w_z$ . To fulfill the second condition, the remaining width  $w_y$  has to be larger than  $w_x, w_z$  (see section 1.4.1). This leads to cigar-shaped traps which are placed side by side (see figure 6.3, we chose the trap aspect ratio  $w_z/w_y = 1/8$ ). This geometry also turns out to be the most “convenient” for the experiment (see appendix A.2). We have provided supplementary calculations with different aspect ratios in appendix B.

**Depth of the potential:** For the depth of the potential there are also certain limitations. If  $V_0$  is too low, the potential is not able to trap the particles. If it is too large, the tunneling rate is too low (see above). It turns out that  $\tilde{V}_0 = V_0/\epsilon = 80$  is a reasonable value<sup>12</sup> which allows a large variety of states.

### 6.3.2. Interaction parameters

We simulate the dimensionless Gross-Pitaevskii equation as stated in (1.10). If all parameters of the external potential are known, there are only two quantities left which

<sup>10</sup>The reason is simply that the particle interchange is reduced and it takes exponentially long to get to the real ground state.

<sup>11</sup>There might be changes in the on-site energy due to “second order” effects: if the changed inter-site coupling leads to a different shape of the on-site wave function. Strictly speaking this condition can only be fulfilled for a single well.

<sup>12</sup>The unit of energy  $\epsilon = \hbar^2/ml^2$  depends on the chosen system. For  $^{52}\text{Cr}$  and  $l = 2\text{ }\mu\text{m}$  we have  $\epsilon \approx 50\text{ Hz} \cdot \hbar$  which leads to a depth of  $V_0 = 4\text{ kHz} \cdot \hbar$  or  $V_0 = 200\text{ }\mu\text{K} \cdot k_B$  which is achievable by an optical dipole trap.

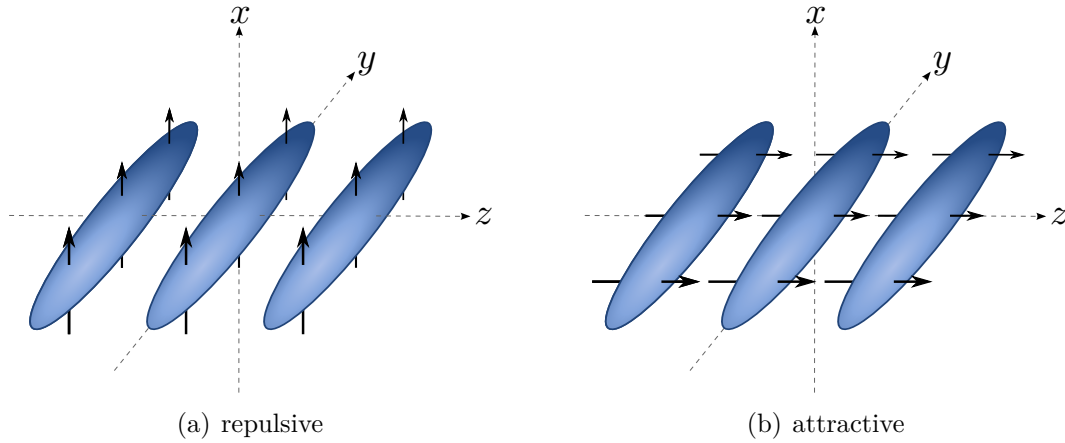


**Figure 6.3.:** Sketch of the geometry which fulfills both conditions: more stable than the spherical case and same on-site energy for both cases (repulsive and attractive inter-site interaction). See text for details.

determine the strength of the contact and dipolar interaction. These are the dimensionless products  $\tilde{a}N = aN/l$  and  $\tilde{a}_{dd}N = a_{dd}N/l$ . Note that it is not necessary to change the number of particles  $N$  independently. In the following we will present several simulations where we scan both parameters to map the whole (remaining) parameter space.

### 6.3.3. Repulsive inter-site energy

Figure 6.4 shows an overview of the states for the geometry with repulsive inter-site interactions. We plot the ratio  $n = (n_1 + n_3)/N$  to indicate the shape of the wave function and keep the analogy to the phase diagrams of the Bose-Hubbard model. We calculate the “occupation numbers” by integrating the density  $n(\mathbf{r})$  over the single wells. To measure  $n_2$ , for example, we sum in the lattice direction from  $-l/2$  to  $l/2$  and over whole area perpendicular to the lattice.

From the Bose-Hubbard model (for  $U_1 \geq 0$  and  $U_0 \geq 0$ ) we expect to find symmetric states with less atoms in the middle ( $n_2 < n_1 = n_3$ ) corresponding to a ratio  $n > 2/3$ . For very strong interactions, phase B showed up with  $n_2 = 0$  corresponding to a ratio of  $n = 1$ . In the numerical simulations we find indeed the whole spectrum  $2/3 \leq n < 1$ . If  $n$  approaches the value of 1, however, the states become unstable<sup>13</sup>. This means we find no equivalent region to phase B.

Having a closer look at the central region of the diagram (figure 6.4(b)) we see that a

---

<sup>13</sup>It should be noted that some states pointed out in the diagram with  $n \approx 1$  or  $n \approx 0$  are in fact unstable. However, they only collapse after a very large number of simulations steps in the imaginary time evolution. It is thus hard to decide numerically if a given state is stable or not. We know that similar problems appear in an experiment, where the collapse time might be larger than the lifetime of a state which is determined by particle losses.

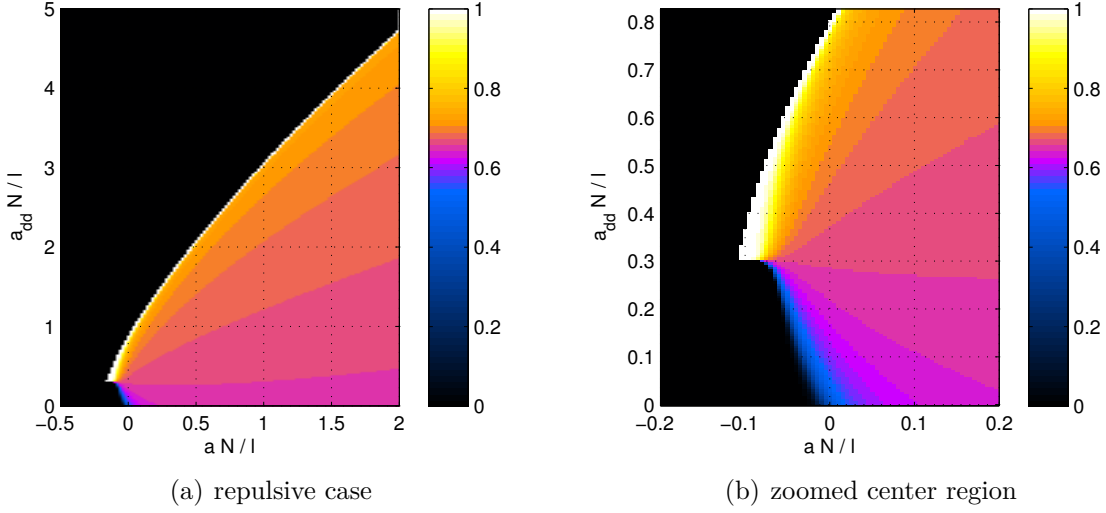


**Figure 6.4.:** The quantity  $n = (n_1 + n_3)/N$  is plotted for the geometry with repulsive inter-site interactions. Black colored areas indicate *regions of instability* where no ground state could be found. For the purely contact-interacting case ( $a_{dd} = 0, a > 0$ ) we find an equally populated state with  $n_1 \approx n_2 \approx n_3$ . For increasing  $a_{dd}$  the state gets slowly closer to the state of “phase B” with  $n_2 = 0, n_1 = n_3 = N/2$  (white). This state only appears close to instability regions. In the center for small  $|a|$  and  $a_{dd}$  we find states with more atoms in the middle (see the non-interacting ground state,  $a = a_{dd} = 0$ ).

threshold value  $a_{dd}N/l \approx 0.3$  exists<sup>14</sup>, below which the ratio  $n$  is always lower than  $2/3$ . This region is dominated by the on-site interactions. For small contact interaction the state approaches the non-interacting state  $n \approx 0.5$  and finally collapses. Two cuts through the diagram, just below and above the threshold value, are shown in figure 6.5(b).

The behavior of the border, separating stable from unstable regions, is also different below and above the threshold. Below, the instability is triggered by a collapse of the middle well as it holds most of the particles. The system gets more stable for higher values of  $a_{dd}N/l$ .

Above the threshold, the instability is caused by the particle flow to the outer wells which finally leads to a collapse in the outer wells (in the simulation we see a collapse either in the left or right well). This is a clear signature of the inter-site effects. Above the threshold, the system gets less stable for growing dipolar strength.

<sup>14</sup>This value is not depending on the geometry but on the depth of the potential (see supplementary calculations in appendix B). For  $^{52}\text{Cr}$  and  $l = 2\text{ }\mu\text{m}$  one needs at least  $N \approx 1000$  atoms to exceed the threshold.

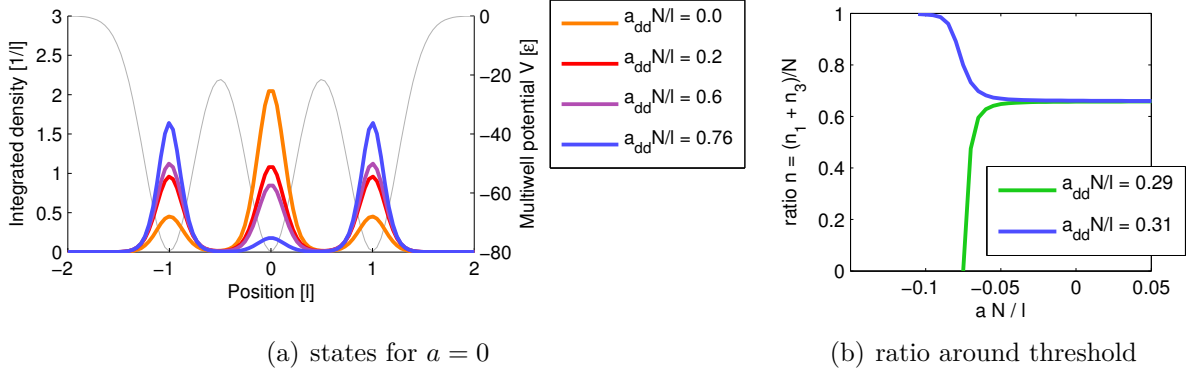


**Figure 6.5.:** (a) Purely dipolar states with  $a = 0$  and different values for  $a_{dd}N/l$  in the repulsive case. Particles move to the outer wells as the dipolar repulsion grows. (b) Ratio  $n = (n_1 + n_3)/N$  for different scattering lengths, just below and above the threshold value of  $a_{dd}N/l \approx 0.3$ . Below the threshold, states always have less atoms in the outer wells ( $n < 2/3$ ). Above the threshold states with  $n \approx 1$  appear close to the collapse point (here:  $aN/l \approx -0.1$ ).

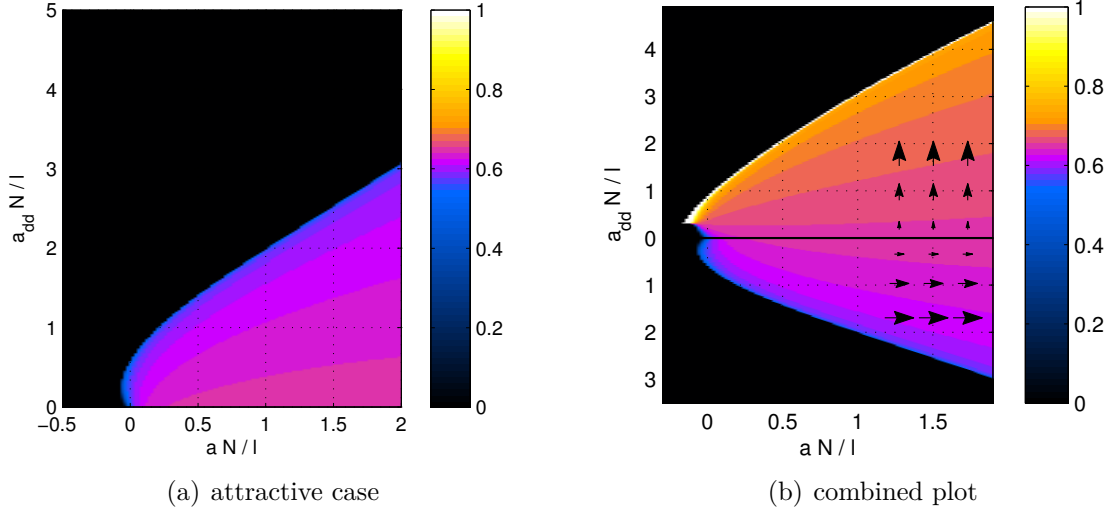
### 6.3.4. Attractive inter-site energy

Figure 6.6(a) shows an overview of the states for the geometry with attractive inter-site interactions. We use again the same quantity  $n$  to indicate the shape of the wave function. Like in the repulsive case we get the whole spectrum of ratios  $n$  which is expected from the Bose-Hubbard model (for phase A). For the attractive case these are the values between the equally populated state with  $n = 2/3$  and the non-interacting state with  $n \approx 0.5$ . Approaching a value of  $n = 0.5$ , the states become unstable. In this situation, the collapse is again triggered by the middle well.

### 6.3.5. Combined picture

Figure 6.6(b) shows a combined plot of both cases (repulsive and attractive inter-site interaction). For  $a_{dd} = 0$  both situations are identical. Differences in the upper and lower part are only due to inter-site effects, as the geometry was chosen in such a way (first condition in section 6.3.1). The image may, with some caution, qualitatively be compared to the phase diagrams of the Bose-Hubbard model or the variational method (figure 4.2 on page 41). Note however that the on-site parameter  $U_0$  in the Bose-Hubbard model depends on both,  $a$  and  $a_{dd}$ .

Within the mean-field theory and our numerical simulations we observe all states of phase A, but none of the phases B, C or D. We conclude that all the regions which correspond to the phases B, C and D are unstable. There are however small regions in the new diagram where the ratio  $n$  is very close to the values in phase B ( $n \approx 1$ ) or



**Figure 6.6.:** (a) The quantity  $n = (n_1 + n_3)/N$  is plotted for the geometry with attractive inter-site interactions. Black color again indicates unstable regions. Close to the instability, states with  $n \approx 0.5$  form which resemble the non-interacting ground state. (b) Combined plot which shows the repulsive case (upper part) and the attractive case (lower part, flipped  $a_{dd}$  axis). Both simulations match exactly if  $a_{dd} = 0$  but also for larger  $a_{dd}$  the plot combines to a consistent picture. The strength and direction of the dipolar interaction is indicated by the small arrows. Differences in both parts are only caused by inter-site effects.

phase D<sup>15</sup> ( $n \approx 0.5$ ). Especially all the states with  $n > 2/3$  (above the threshold value of  $a_{dd}N/l \approx 0.3$ ) do not appear for contact interacting condensates and should therefore be considered as a strong evidence for inter-site interactions.

<sup>15</sup>The states of phase D are  $(N/2|N/2|0)$  and  $(0|N/2|N/2)$  which give a mean ratio of  $n = 0.5$ . In the numerical simulations we see however only the equivalent to the non-interacting state with  $(N/4|N/2|N/4)$  which also has a ratio of  $n = 0.5$ .



# Conclusions and outlook

## Conclusions

Within this thesis we have resumed the work on a dipolar Bose-Einstein condensate in a triple-well potential which was started by Lahaye et al. in [14]. We have extended the Bose-Hubbard model to an arbitrary number of wells (chapter 3) and have solved the simplified case of vanishing tunneling rate with the variational method in chapter 4. With this method we were able to describe the ground states for systems with several additional wells. Analytical solutions for two and three wells have been given and we have compared the variational method with the exact diagonalization of the Bose-Hubbard Hamiltonian. In both cases we find four distinct phases of the triple-well system, depending on the sign and strength of the on-site and inter-site interactions. Especially for large dipolar interactions we find ground states which clearly reveal the nonlocal character of the interaction. An extreme case is realized in phase B for repulsive inter-site interactions. In this state all particles are distributed evenly in the outer two wells and the middle well is completely emptied.

Both methods are only applicable in the regime of small particle numbers. We showed this in chapter 5 where we have calculated how the on-site energy in a contact-interacting condensate scales with the number of atoms. We proved that, for a large number of particles, the scaling exponent  $\frac{4+d}{2+d}$  depends only on the dimensionality  $d$ . The exponent is universal and independent from the chosen regime (Gaussian ansatz or Thomas-Fermi approximation). The analytical calculations are supported by numerical simulations. Only for  $d = 0$  the scaling matches the quadratic behavior of the Bose-Hubbard model.

The modified scaling was one motivation to head on and take another approach to investigate the multi-well system. We have simulated the dipolar Gross-Pitaevskii equation on a three dimensional grid using the split-step method and the technique of imaginary time evolution. We took care of all experimental conditions known so far. For repulsive as well as attractive inter-site interactions we could find qualitative agreement with our previous model, in the sense that we recover the whole spectrum of states. However, the interesting states which were previously found to be existing in a large region of the phase diagram (like the phase B states with an empty central well) only appear close to the instability border, an aspect which is completely neglected in the Bose-Hubbard model.

## Outlook

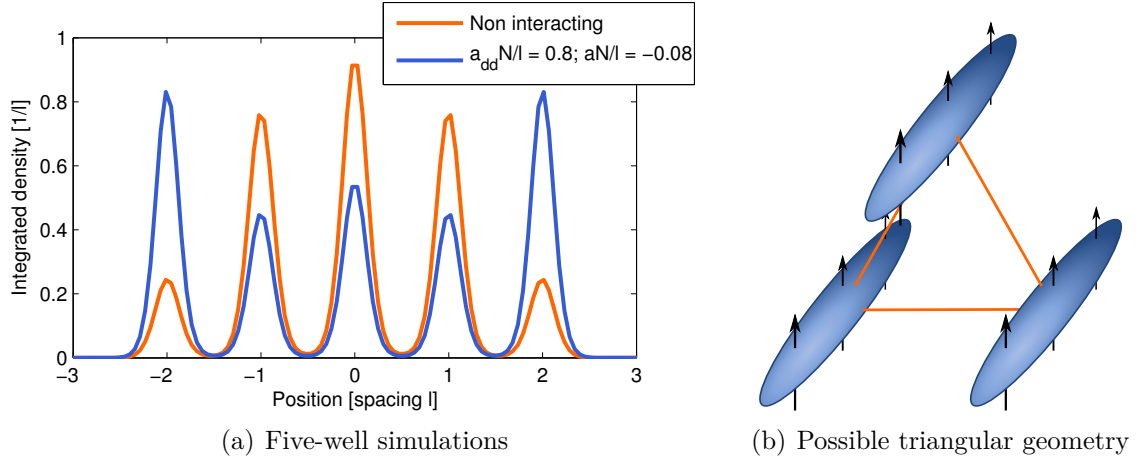


**Figure 6.7.:** (a) Ground states of a system with five wells. For strong dipolar interaction  $a_{dd}N/l = 0.8$  and negative contact interaction  $aN/l = -0.08$  the ground state shows an oscillating distribution of the atoms in the five wells. (b) Three wells which are aligned on an equilateral triangle could serve as a model system for 2D lattices.

The methods and tools provided in this thesis are suited to be extended to a broader scope of problems.

Once all parameters of the planned experiment are known, more detailed studies can be arranged to analyze the triple-well situation. Not only the ground states are accessible with our program. Dynamical simulations with a time-dependent potential can be performed to investigate and optimize the loading process of the multi-well potential (adiabaticity). Dynamical processes within the system can also be studied, like the second-order tunneling presented in [14]. First tests show that this effect might be difficult to observe since the system crosses unstable regions during the evolution.

The stability of the system and especially the collapse dynamics are worth to be explored separately. The states with less atoms in the middle well show some analogy to the biconcave structured ground states associated with the roton-maxon spectrum which also undergo a non-trivial collapse [43].

Further directions could be the investigation of other geometries. Not only the extension to more wells is possible but also different alignments of the three wells (see figure 6.7). A triangular geometry could be a model system for two dimensional lattices. In an equilateral triangle, the symmetry between the three wells is only broken by the dipolar interaction. Different interaction arrangements can be designed, depending on the angle of polarization.



# A. Experimental parameters

*This chapter gives an overview of realistic values for certain quantities of dipolar systems based on existing and planned experimental setups. We compare different dipolar species like atoms with a permanent magnetic dipole moment or polar molecules with an electrical dipole moment.*

*The limitations of realizable trapping potentials are also taken into account. The separation between two different wells or the depth of the potential are crucial quantities. Most parameters are chosen such that they match most closely with the planned experiment of our group.*

## A.1. Dipolar gases

The selection of dipolar systems in this chapter is by no means complete (for an overview see [20]). We present a few examples to demonstrate that our chosen parameters are in agreement with experimentally realizable conditions.

Most of the existing experiments on ultracold gases are using alkali atoms. We include them as a reference. All alkali atoms have a permanent magnetic dipole moment of  $1\mu_B$  where the Bohr magneton is given by  $\mu_B = \frac{e\hbar}{2m_e}$  with the electron mass  $m_e$  and elementary charge  $e$ . It is a practical unit to measure atomic dipole moments (of magnetic origin).

There are also several existing experiments using atomic species with particularly high magnetic dipole moments such as  $^{52}\text{Cr}$  with a magnetic moment of  $6\mu_B$  [5] or  $^{164}\text{Dy}$  with the highest known magnetic moment of  $10\mu_B$  [44].

To compare both magnetic and electric dipoles we choose as a quantitative measure the dipolar length

$$a_{\text{dd}} = \frac{m}{4\pi\hbar^2} g_{\text{dd}} = \frac{m}{\hbar^2} \frac{C_{\text{dd}}\mu^2}{3} = \begin{cases} \frac{m}{12\pi\hbar^2} \cdot \mu_0\mu^2, & \text{for magnetic dipoles.} \\ \frac{m}{12\pi\hbar^2} \cdot \frac{\mu^2}{\epsilon_0}, & \text{for electric dipoles.} \end{cases}$$

Typical electric dipole moments<sup>1</sup> of polar molecules are of the order of 1 Debye =  $1\text{ D} \approx 3.34 \cdot 10^{-30}\text{ C m}$  [45]. Thus, neglecting the effect of the mass, the interaction between electrical dipoles is typically

$$\frac{(1\text{ D})^2/\epsilon_0}{\mu_0(1\mu_B)^2} \approx 10^5$$

---

<sup>1</sup>Note that dipole moment of a heteronuclear molecule in its rovibrational ground state is zero due to the rotational symmetry. By applying an electric field, however, the molecules get oriented and higher states with non vanishing dipole moment are admixed.

isotope	scattering length $a$ [ $a_0$ ]	dipolar length $a_{\text{dd}}$ [ $a_0$ ]
$^{87}\text{Rb}$	110	0.7
$^{52}\text{Cr}$	105	15
$^{164}\text{Dy}$	$\lesssim 130$	134

**Table A.1.:** Experimental values for the background scattering length  $a$  and the dipolar length  $a_{\text{dd}}$  for some chosen atoms. Both lengths are measured in units of the Bohr radius  $a_0 \approx 53$  pm. Values taken from [19, 25, 44].

times stronger than between magnetic dipoles. Even when compared to dysprosium the dipolar lengths of polar molecules are still 1000 times larger. For such strong interactions it is questionable if our mean field approach is still valid. Therefore we will only consider atomic species with magnetic dipole moments throughout this work. Table A.1 gives an overview of the scattering length and the dipolar length for different atoms.

## A.2. Interaction parameters

For the simulations within a multi-well potential we are interested in the dimensionless interaction parameters  $\tilde{a}N = aN/l$  and  $\tilde{a}_{\text{dd}}N = a_{\text{dd}}N/l$  where  $l$  is the separation between two wells (see section 1.3.3 for details). In the following we will give reasonable ranges of values for all quantities. The minimum and maximum values for both interaction parameters which can be achieved with these ranges of values are summarized in table A.2.

**Spacing:** Both for an optical lattice (where the lattice spacing  $l = \lambda/2$  is half the wavelength of the counter-propagating beams) and for an optical potential created by a deflected laser beam, the spacing between two wells is of the order of  $1\text{ }\mu\text{m}$ . For the planned experiment, the spacing will be approximately  $l = 2\text{ }\mu\text{m}$  [14].

**Number of atoms:** The total number of atoms which can be loaded into the multi-well potential is limited by the cooling process [36, section 3.1.2]. The maximum achievable value will probably be  $N_{\text{max}} \approx 20,000$ . The minimum is limited by technical issues (loading and detection) and is approximately  $N_{\text{min}} \approx 300$ .

**Scattering length:** As mentioned in the motivation, the scattering length is not a fixed quantity but can be tuned by means of Feshbach resonances [4]. In the presence of a resonance, the scattering length can in principle be tuned to arbitrary values. In practice, the uncertainty  $\Delta a$  is the crucial quantity which depends on the width of the resonance and technical details. For chromium, a reasonable range for the scattering length is  $-a_{\text{BG}}$

particles $N$	contact interaction $aN/l$		dipolar interaction $a_{\text{dd}}N/l$	
	300	20,000	300	20,000
$^{87}\text{Rb}$	0.9	58	0.006	0.4
$^{52}\text{Cr}$	0.8	56	0.1	8
$^{164}\text{Dy}$	$\lesssim 1.0$	67	1.1	71

**Table A.2.:** Overview of interaction parameters  $aN/l$  and  $a_{\text{dd}}N/l$  for different number of atoms. The values given for the contact interaction parameter can be tuned by means of Feshbach resonances. Alkali atoms such as rubidium are not suited to study the dipolar multi-well system since the maximum achievable  $a_{\text{dd}}N/l$  hardly reaches the threshold value to see phase B states (see section 6.3.3). Dysprosium has the most promising ratio  $a_{\text{dd}}/a$  to scan the phase diagram (if the scattering length is tunable, there are no known Feshbach resonances so far).

to  $a_{\text{BG}}$  with a resolution<sup>2</sup> of roughly  $\Delta a = 2a_0$ , where  $a_{\text{BG}} \approx 105a_0$  is the background scattering length [36, section 3.2.1].

**Dipolar length:** The permanent dipole moment is fixed and the dipolar length  $a_{\text{dd}}$  can thus not be tuned. However, the inter-site interaction may be tuned smoothly by changing the polarization angle. For our simulations we have only considered the geometries with a polarization axis which matches one of the symmetry axis. In principle, arbitrary angles can be realized. Due to the finite size of the single condensates, the relation between the angle and the size of the inter-site energy, however, is not trivial (see section 2.2).

### A.3. The single wells

**Geometry:** The single wells of the multi-well potential will be created by focused laser beams [15, section 4.2]. The profile of the beam is spherical and has a waist of  $w_\rho = 1 \mu\text{m}$ . The width in the propagation direction is given by the Rayleigh range  $z_{\text{R}} = \pi w_\rho^2 / \lambda \approx 6 \mu\text{m}$ , where  $\lambda = 532 \text{ nm}$  is the wavelength of the beam. The shape of the single wells is therefore cigar-like with an aspect ratio of  $w_\rho/w_z = \omega_z/\omega_\rho \approx 1/6$ . Simulations for different aspect ratios are provided in appendix B.1.

**Depth:** The depth of the single wells is determined by the power of the laser beams, the scattering rate, the detuning and details of the atomic transitions. It is one of the parameters which can be widely tuned and in principle the whole range from 0 to several hundred  $\epsilon$  is accessible ( $\epsilon = \hbar^2/ml^2$  is the unit of energy).

<sup>2</sup>The uncertainty  $\Delta a$  depends on the value of  $a$  and is very small around  $a_{\text{BG}}$  but gets much larger close to the resonance. For  $-a_{\text{BG}}$  the resolution is approximately  $\Delta a = 10a_0$ .



## B. Supplementary calculations

*In this appendix we provide some additional numerical simulations which were performed to cover a wider range of parameters.*

*For the simulations in the main part of the thesis we used some parameters which were given by experimental conditions. We show that our basic picture and description does not change if the restrictions are loosened and some of the important parameters are changed. Two parameters in particular, the aspect ratio of the single wells and the depth of the multi-well potential, were set to one single set of experimentally realizable values. However, both can be tuned in the experiment.*

### B.1. Changed aspect ratio

Together with the simulation from the main part, we ran simulations for the following aspect ratios of the single wells (see appendix A.2 for the definition):  $\omega_z/\omega_\rho = 1/8, 1/4$  and 1. The results are presented in figure B.1. We observe that the threshold value of  $a_{\text{dd}}N/l \approx 0.3$ , introduced in section 6.3.3 does not change with the aspect ratio. There is however a significant change in the stability of the system. For repulsive inter-site interactions (above the threshold value), the stability decreases with increasing aspect ratio (wells become more spherical). This can be explained as follows. As described, the instability above the threshold is triggered by inter-site effects. As the inter-site interaction grows with the aspect ratio (see section 2.2.1 for a similar discussion), the instability occurs for smaller  $a_{\text{dd}}N/l$ .

For the stability border on the attractive site of the diagram the same arguments apply. The effect is the same but much weaker. For the spherical case we see that the stability curve is roughly symmetric with respect to the  $aN/l$  axis.

### B.2. Changed depth of the potential

We decreased also the trap depth from  $V_0/\epsilon = 80$  to a value of 40. The stability curve is not affected since the stability is mainly connected with the geometry of the single wells. When changing the depth, the single trapping frequencies are altered but the aspect ratio is constant.

We see however an effect on the threshold value which increases to  $a_{\text{dd}}N/l \approx 0.65$  for a depth of  $V_0/\epsilon = 40$ .

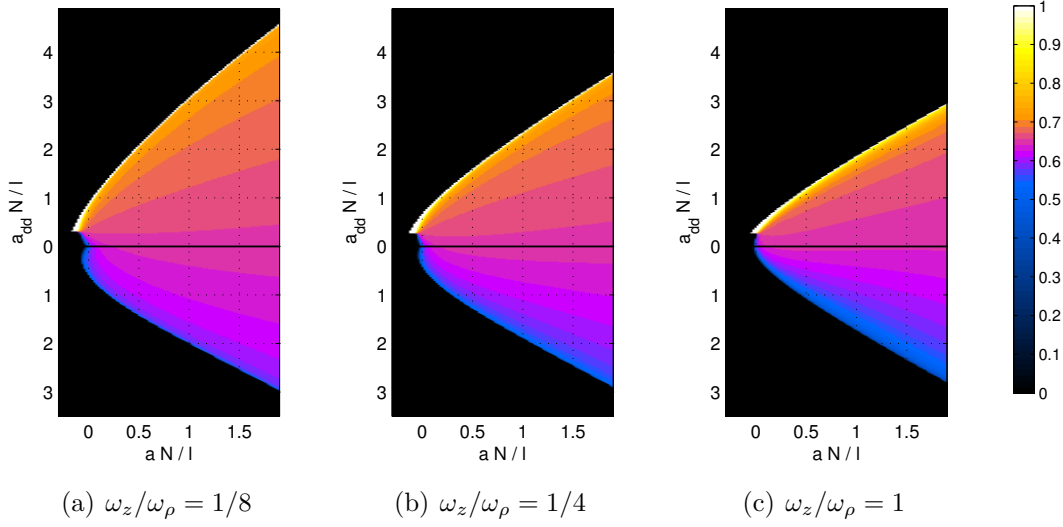


**Figure B.1.:** The same simulation which was described in section 6.3, for changed aspect ratios of the single wells ( $\omega_z/\omega_\rho = 1/8$  is the reference). The threshold value of  $a_{dd}N/l \approx 0.3$  does not change. For increasing aspect ratio (left to right), the system gets less stable for repulsive inter-site interactions (upper part). For attractive inter-site interactions the stability is hardly affected but the transition to the  $n = 1/2$  states is smoother (lower part).

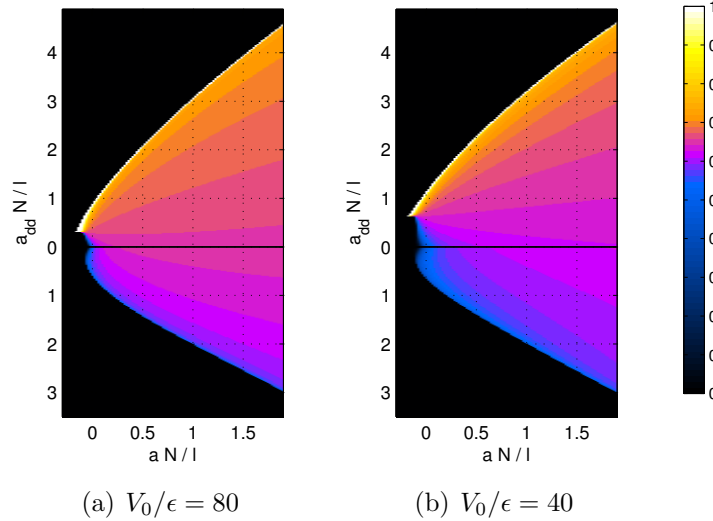


**Figure B.2.:** Simulations for two different trap depths ( $V_0/\epsilon = 80$  is the reference). The stability curve is not affected by the change of the depth but the threshold value increases to  $a_{dd}N/l \approx 0.65$  for a depth of  $V_0/\epsilon = 40$ .

## C. Documentation of the simulation program

*This chapter gives an overview of the concept and a technical documentation of the program which is simulating the dipolar Gross-Pitaevskii equation. The core of the program is written in C++. It is configured and controlled by a Python scripting interface which is an easy way to extend the functionality of the main program without writing low-level code.*

*The kernel implements all the basic functionality like data storage and manipulation, fast Fourier transforms, a parameter database, file I/O and more. The code is parallelized in large parts and is ready for application on multi-core CPUs.*

*The python layer is mostly responsible for parameter setting, unit conversion, sequential control and batch processing. Modules for several different simulation types exist.*

### C.1. Concept and structure

As outlined in the introduction, the simulation program is divided into two parts. The main program is written in pure C++ and handles all performance critical low-level features. The code is parallelized using OpenMP [46]. We use the boost::python library to provide an interface to the Python scripting language [47]. The parts written in Python are not relevant for the overall performance. They include setting the initial parameters, controlling the simulated sequence or computing and writing out different quantities.

Both parts of the program are designed with an object oriented structure (figure C.1 shows the logical connections and inheritance lines of all important classes). The C++ core holds a general class `Field` for objects which are defined on the 3D grid<sup>1</sup>, the child class `Array` which stores complex numbers for each grid point and provides a lot of methods for converting and copying data, computing different quantities, Fourier transforming<sup>2</sup> and writing cuts or projections. The `Array` class provides an interface for both the `Wavefunction` class and all constant objects like the external potential `PotentialExternal` or the Fourier transformed dipolar potential `PotentialDipolar`. The `Wavefunction` class has methods for the propagation in real or imaginary time (see 6.1.2 for details on the evolution) and has subclasses for different initial wave functions (`WavefunctionGaussian` and `WavefunctionRandom`).

---

<sup>1</sup>And the derived class `FieldConstant` for constant quantities

<sup>2</sup>The FFTW library is used for parallelized fast Fourier transforms [48].

The main evolution steps and the initialization is managed by the class `Simulation`. A general parameter database and functions for calculating the grid properties is provided by `SimulationParameters`. The class `GPEPython` is a wrapper class to export all public methods to a Python module.

On the Python side the class `GPE` inherits all functions from the C++ interface and adds some features for running and managing simulations. There are subclasses for special types of simulations (`HarmonicTrapGPE` and `LatticeGPE`).

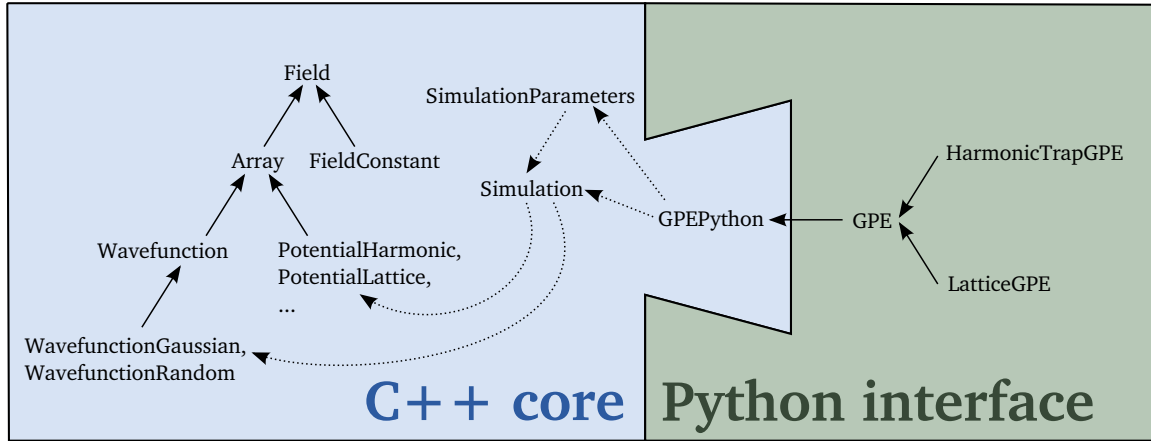


**Figure C.1.:** Schematic structure of the simulation program. Solid arrows are real inheritances, dotted arrows symbolize logical connections. The C++ kernel implements all low-level features while the Python interface is used to script the single simulations. The `GPEPython` wrapper class provides an interface to the Python layer.

## C.2. Setting up the program

This section gives a short summary on how to run a simple simulation via the Python interface. We assume that all the necessary software and libraries are installed.

### Requirements

To compile the program the following compilers and libraries are needed<sup>3</sup>: GCC 4.5 or higher<sup>4</sup>, Python 2.6 or higher, libboost-python 1.42 or higher, FFTW 3.2.2 or higher.

<sup>3</sup>Lower version numbers *might* be working.

<sup>4</sup>Comparable C++ compiler with OpenMP and C++0x features enabled should be working. Program was also compiled using the Intel C Compiler.



## Example simulation

The following Python script C.1 demonstrates a basic simulation in a harmonic external potential. All parameters which are not set explicitly have default values defined in `HarmonicTrapGPE`. Parameters have units as defined in section 1.3.3. The scattering length  $a$  and the dipolar length  $a_{\text{dd}}$ , for example, are measured in units of the harmonic oscillator length.

---

**Listing C.1:** Python script running a simple simulation

---

```
1 from gpe import HarmonicTrapGPE, GPE
2
3 # Initialize the GPE simulation
4 # Parameters are the name and trapping frequencies
5 # in x, y, z direction
6 sim = HarmonicTrapGPE("Harmonic_Trap_Simulation", 1.0, 1.0, 1.0)
7
8 # Set size of grid (128 x 128 x 128)
9 sim.setGridSize(128)
10
11 # Contact and dipolar interaction parameters
12 sim.set("atomNumber", 2000)
13 sim.set("scatteringLength", 0.001)
14 sim.set("dipolarLength", 0.001)
15
16 # Initialize all parameters and arrays
17 sim.initialize()
18
19 # Run imaginary time evolution for 10000 steps,
20 # write energies every 100 steps
21 sim.ite(10000, 100)
22
23 # Print out cuts / projections of the final state
24 sim.write("final")
```

---

To run the script, the `gpe.py` module and the `gpepython.so` library have to be in the same folder or on the Python path.

## C.3. Scripting interface

This section gives a short summary of the most important (Python side) methods to modify and control a simulation. For further details see the inline documentation of the `gpe.py` module.

## GPE class

The GPE class is the basic python interface to the simulation program.

**GPE.\_\_init\_\_(self, name)**

Constructor of the GPE class, initializes the GPE simulation object. **name** is a descriptor for this simulation and will be used as the name of a directory where the results will be stored.

**GPE.set(self, name, value)**

Set certain simulation parameters. **name** is the descriptor for the variable and **value** the double precision value. There exist similar methods to set boolean parameters (**setBool**) and string parameters (**setString**).

**GPE.setGrid(self, sizeX, sizeY, sizeZ)**

Sets the grid size. **sizeX** is the number of grid points in  $x$  direction. The same for **sizeY** and **sizeZ**. If the latter are not given, a symmetric grid is assumed.

**GPE.setMax(self, maxX, maxY, maxZ)**

Sets the grid extension. **maxX** is the maximum extension in  $x$  direction. The same for **maxY** and **maxZ**. If the latter are not given, a symmetric grid is assumed.

**GPE.initialize(self, name, deleteWavefunction)**

Initializes the simulation (creates the grid and all arrays like the external potential), has to be called prior to **rte** or **ite**. Also has to be used if certain quantities are changed which require reinitialization of the grid or stored arrays like parameters of the external potential. The boolean switch **deleteWavefunction** determines whether the wave function object is also initialized. Should normally be set to **False** if parameters are changed *during* the simulation, but set to **True** for the first initialization (default).

**GPE.ite(self, steps, monitorSteps, plotSteps)**

Run the imaginary time evolution for a certain number of steps, monitor the energy every **monitorSteps** steps and write projections every **plotSteps** steps.

**GPE.rte(self, steps, monitorSteps, plotSteps)**

Run the real time evolution for a certain number of steps, monitor the energy every **monitorSteps** steps and write projections every **plotSteps** steps.

**GPE.evolution(self, steps, monitorSteps, plotSteps)**

Run the simulation for a certain number of steps (**steps**), monitor the energy every **monitorSteps** steps and write projections every **plotSteps** steps. See also **evolutionType** property. The methods **ite** and **rte** should be used as wrappers for imaginary / real time evolution.

**GPE.evaluate([self](#), quantity)**

Computes certain quantities. **quantity** is an integer parameter with some predefined values: **DISPERSION\_X** calculates the dispersion of the wave function in  $x$  direction, the same for  $y$  and  $z$ . **PSI\_POWER\_2** calculates the norm of the wave function  $\int d^3r |\Psi|^2$ . **PSI\_POWER\_6** calculates the same integral with the sixth power of the wave function (density cubed, for three body properties). **PSI\_0RE** and **PSI\_0IM** give the real and imaginary value of  $\Psi$  in the center of the grid, respectively.

**GPE.energy([self](#))**

Returns the total energy  $E_{\text{tot}} = E_{\text{kin}} + E_{\text{pot}} + E_{\text{con}} + E_{\text{dip}}$ . There exist several methods to extract only certain parts of the energy: **energyKinetic**, **energyPotential**, **energyContact**, **energyDipolar**.

**GPE.virial([self](#))**

Returns the virial  $V = 2(E_{\text{kin}} - E_{\text{pot}}) + 3(E_{\text{con}} + E_{\text{dip}})$ .

**GPE.write([self](#), name)**

Write out some predefined 1D and 2D cuts and projections to data files in the simulation folder. **name** is the prefix of the output files.

**GPE.writePotential([self](#), name)**

Write out some predefined 1D and 2D cuts and projections of the external potential. **name** is the prefix of the output files.

**GPE.get([self](#), name)**

Read simulation parameters values. **name** is the descriptor for the variable. There exist similar methods to get boolean parameters (**getBool**) and string parameters (**getString**).

**GPE.setThreads([self](#), nthreads)**

Set the number of threads which should be used to run the simulation. Typically this should not exceed the number of CPU cores. Can also be set by the environmental variable **OMP\_NUM\_THREADS**.

## HarmonicTrapGPE class

This class is a subclass of **GPE**. It is suited to run a simulation with a harmonic trap as external potential. It uses oscillatory units (defined by the trapping frequency in  $z$  direction) as defined in section 1.3.3.

**HarmonicTrapGPE.\_\_init\_\_(self, name, omegaX, omegaY, omegaZ)**

Constructor of the class, initializes the simulation, see constructor of super class GPE.\_\_init\_\_(self, name). It sets the trap parameters ( $\omega_x, \omega_y$  and  $\omega_z$ ). Calculates reasonable maxX, maxY and maxZ parameters as well as starting values  $\sigma_i = \sqrt{\hbar/m\omega_i}$  for the extension of the Gaussian wave function sigmaX, sigmaY and sigmaZ according to the harmonic oscillator lengths in the different directions.

## LatticeGPE class

This class is a subclass of GPE. It is suited to run a simulation in a Gaussian multi-well potential as defined in section 2.1. As a length scale the spacing between the wells is used.

**LatticeGPE.\_\_init\_\_(self, name, lSites, lDirection, lDepth, lWidth)**

Constructor of the class, initializes the simulation, see constructor of super class GPE.\_\_init\_\_(self, name). Sets the trap parameters: lSites is the number of wells or lattice sites  $N_S$ , lDirection is the lattice direction which can be 0 ( $x$ ), 1 ( $y$ ) or 2 ( $z$ ). lDepth is the parameter  $V_0$  and lWidth can be either a single value or an array of the parameters  $w_x, w_y, w_z$ .

## Parameters

The following list is an overview of the most important simulation parameters.

Parameter name	Type	Description
sizeX, sizeY, sizeZ	double	Number of grid points in $x, y$ and $z$ direction, respectively
maxX, maxY, maxZ	double	Extension of the grid in the different spacial directions
timeStep	double	The time step $\Delta t$ .
atomNumber	double	The number of atoms $N_A$ .
scatteringLength	double	The scattering length $a$ .
dipolarLength	double	The dipolar length $a_{dd}$ .
evolutionKinetic	bool	Whether or not the evolution due to kinetic energy is switched on
evolutionExternal	bool	The same for the external potential
evolutionContact	bool	The same for the contact interaction
evolutionDipolar	bool	The same for the dipolar interaction
externalPotential	string	The type of external potential (“harmonic”, “modulatedHarmonic” or “lattice”)

# Bibliography

- [1] M. Anderson, J. Ensher, M. Matthews, C. Wieman and E. Cornell, *Observation of Bose-Einstein condensation in a dilute atomic vapor*, Science, **269**, 198 (1995).
- [2] K. B. Davis, M. O. Mewes, M. R. Andrews, N. J. van Druten, D. S. Durfee, D. M. Kurn and W. Ketterle, *Bose-Einstein Condensation in a Gas of Sodium Atoms*, Phys. Rev. Lett., **75**, 3969–3973 (1995).
- [3] C. C. Bradley, C. A. Sackett, J. J. Tollett and R. G. Hulet, *Evidence of Bose-Einstein Condensation in an Atomic Gas with Attractive Interactions*, Phys. Rev. Lett., **75**, 1687–1690 (1995).
- [4] C. Chin, R. Grimm, P. Julienne and E. Tiesinga, *Feshbach resonances in ultracold gases*, Rev. Mod. Phys., **82**, 1225–1286 (2010).
- [5] A. Griesmaier, J. Werner, S. Hensler, J. Stuhler and T. Pfau, *Bose-Einstein Condensation of Chromium*, Phys. Rev. Lett., **94**, 160401 (2005).
- [6] T. Lahaye, T. Koch, B. Frohlich, M. Fattori, J. Metz, A. Griesmaier, S. Giovanazzi and T. Pfau, *Strong dipolar effects in a quantum ferrofluid*, Nature, **448**, 672–675 (2007).
- [7] T. Lahaye, J. Metz, B. Fröhlich, T. Koch, M. Meister, A. Griesmaier, T. Pfau, H. Saito, Y. Kawaguchi and M. Ueda, *d-Wave Collapse and Explosion of a Dipolar Bose-Einstein Condensate*, Phys. Rev. Lett., **101**, 080401 (2008).
- [8] T. Koch, T. Lahaye, J. Metz, B. Frohlich, A. Griesmaier and T. Pfau, *Stabilization of a purely dipolar quantum gas against collapse*, Nature Physics, **4**, 218–222 (2008).
- [9] S. Müller, J. Billy, E. A. L. Henn, H. Kadau, A. Griesmaier, M. Jona-Lasinio, L. Santos and T. Pfau, *Dipolar Stabilization of an Attractive Bose Gas in a One Dimensional Lattice*, arXiv:1105.5015 (2011).
- [10] L. Santos, G. V. Shlyapnikov and M. Lewenstein, *Roton-Maxon Spectrum and Stability of Trapped Dipolar Bose-Einstein Condensates*, Phys. Rev. Lett., **90**, 250403 (2003).
- [11] S. Ronen, D. C. E. Bortolotti and J. L. Bohn, *Radial and Angular Rotons in Trapped Dipolar Gases*, Phys. Rev. Lett., **98**, 030406 (2007).

- [12] M. Greiner, O. Mandel, T. Esslinger, T. W. Hansch and I. Bloch, *Quantum phase transition from a superfluid to a Mott insulator in a gas of ultracold atoms*, Nature, **415**, 39–44 (2002).
- [13] K. Góral, L. Santos and M. Lewenstein, *Quantum Phases of Dipolar Bosons in Optical Lattices*, Phys. Rev. Lett., **88**, 170406 (2002).
- [14] T. Lahaye, T. Pfau and L. Santos, *Mesoscopic Ensembles of Polar Bosons in Triple-Well Potentials*, Phys. Rev. Lett., **104**, 170404 (2010).
- [15] P. Weinmann, *Setting up a high-resolution optical system for trapping and imaging ultracold chromium atoms*, Diploma thesis, 5. Physikalisches Institut, Universität Stuttgart (2011).
- [16] C. Pethick and H. Smith, *Bose-Einstein condensation in dilute gases*, Cambridge University Press (2002).
- [17] F. Dalfovo, S. Giorgini, L. P. Pitaevskii and S. Stringari, *Theory of Bose-Einstein condensation in trapped gases*, Rev. Mod. Phys., **71**, 463–512 (1999).
- [18] L. Pitaevskii and S. Stringari, *Bose-Einstein condensation*, International series of monographs on physics, Clarendon Press (2003).
- [19] Y. Castin, *Course 1: Bose-Einstein Condensates in Atomic Gases: Simple Theoretical Results*, in R. Kaiser, C. Westbrook, & F. David, editor, *Coherent Atomic Matter Waves* (2001).
- [20] T. Lahaye, C. Menotti, L. Santos, M. Lewenstein and T. Pfau, *The physics of dipolar bosonic quantum gases*, Reports on Progress in Physics, **72**, 126401 (2009).
- [21] D. O’Dell, S. Giovanazzi, G. Kurizki and V. M. Akulin, *Bose-Einstein Condensates with  $1/r$  Interatomic Attraction: Electromagnetically Induced “Gravity”*, Phys. Rev. Lett., **84**, 5687–5690 (2000).
- [22] J. D. Jackson, *Classical Electrodynamics Third Edition*, Wiley, third edition (1998).
- [23] L. Santos, G. V. Shlyapnikov, P. Zoller and M. Lewenstein, *Bose-Einstein Condensation in Trapped Dipolar Gases*, Phys. Rev. Lett., **85**, 1791–1794 (2000).
- [24] K. Góral, K. Rzażewski and T. Pfau, *Bose-Einstein condensation with magnetic dipole-dipole forces*, Phys. Rev. A, **61**, 051601 (2000).
- [25] J. Metz, *Collapse of dipolar Bose-Einstein condensates for different trap geometries*, Ph.D. thesis, Universität Stuttgart (2010).

- 
- [26] C. Eberlein, S. Giovanazzi and D. H. J. O'Dell, *Exact solution of the Thomas-Fermi equation for a trapped Bose-Einstein condensate with dipole-dipole interactions*, Phys. Rev. A, **71**, 033618 (2005).
- [27] A. Gammal, T. Frederico and L. Tomio, *Critical number of atoms for attractive Bose-Einstein condensates with cylindrically symmetrical traps*, Phys. Rev. A, **64**, 055602 (2001).
- [28] S. Giovanazzi, P. Pedri, L. Santos, A. Griesmaier, M. Fattori, T. Koch, J. Stuhler and T. Pfau, *Expansion dynamics of a dipolar Bose-Einstein condensate*, Phys. Rev. A, **74**, 013621 (2006).
- [29] M. Andrews, C. Townsend, H. Miesner, D. Durfee, D. Kurn and W. Ketterle, *Observation of interference between two Bose condensates*, Science, **275**, 637 (1997).
- [30] A. Smerzi, S. Fantoni, S. Giovanazzi and S. R. Shenoy, *Quantum Coherent Atomic Tunneling between Two Trapped Bose-Einstein Condensates*, Phys. Rev. Lett., **79**, 4950–4953 (1997).
- [31] M. Albiez, R. Gati, J. Fölling, S. Hunsmann, M. Cristiani and M. K. Oberthaler, *Direct Observation of Tunneling and Nonlinear Self-Trapping in a Single Bosonic Josephson Junction*, Phys. Rev. Lett., **95**, 010402 (2005).
- [32] R. Grimm, M. Weidemüller and Y. B. Ovchinnikov, *Optical Dipole Traps for Neutral Atoms*, in B. Bederson and H. Walther, editors, *Advances in Atomic Molecular and Optical Physics*, volume 42 of *Advances In Atomic, Molecular, and Optical Physics*, pages 95 – 170, Academic Press (2000).
- [33] M. Fattori, G. Roati, B. Deissler, C. D'Errico, M. Zaccanti, M. Jona-Lasinio, L. Santos, M. Inguscio and G. Modugno, *Magnetic Dipolar Interaction in a Bose-Einstein Condensate Atomic Interferometer*, Phys. Rev. Lett., **101**, 190405 (2008).
- [34] M. Klawunn, A. Pikovski and L. Santos, *Two-dimensional scattering and bound states of polar molecules in bilayers*, Phys. Rev. A, **82**, 044701 (2010).
- [35] S. Giovanazzi, A. Görlitz and T. Pfau, *Tuning the Dipolar Interaction in Quantum Gases*, Phys. Rev. Lett., **89**, 130401 (2002).
- [36] H. Kadau, *A Dipolar Bose-Einstein Condensate in a one-dimensional Optical Lattice*, Diploma thesis, 5. Physikalisches Institut, Universität Stuttgart (2011).
- [37] D. Jaksch, C. Bruder, J. I. Cirac, C. W. Gardiner and P. Zoller, *Cold Bosonic Atoms in Optical Lattices*, Phys. Rev. Lett., **81**, 3108–3111 (1998).
- [38] I. Bloch, J. Dalibard and W. Zwerger, *Many-body physics with ultracold gases*, Rev. Mod. Phys., **80**, 885–964 (2008).

- [39] O. Morsch and M. Oberthaler, *Dynamics of Bose-Einstein condensates in optical lattices*, Rev. Mod. Phys., **78**, 179–215 (2006).
- [40] T. Lahaye, T. Pfau and L. Santos, *Erratum: Mesoscopic Ensembles of Polar Bosons in Triple-Well Potentials [Phys. Rev. Lett. 104, 170404 (2010)]*, Phys. Rev. Lett., **105**, 239904 (2010).
- [41] Z. Hadzibabic and J. Dalibard, *Two-dimensional Bose fluids: An atomic physics perspective*, arXiv:0912.1490 (2009).
- [42] M. L. Chiofalo, S. Succi and M. P. Tosi, *Ground state of trapped interacting Bose-Einstein condensates by an explicit imaginary-time algorithm*, Phys. Rev. E, **62**, 7438–7444 (2000).
- [43] R. M. Wilson, S. Ronen and J. L. Bohn, *Angular collapse of dipolar Bose-Einstein condensates*, Phys. Rev. A, **80**, 023614 (2009).
- [44] M. Lu, N. Q. Burdick, S. H. Youn and B. L. Lev, *A Strongly Dipolar Bose-Einstein Condensate of Dysprosium*, arXiv:1108.5993 (2011).
- [45] K.-K. Ni, S. Ospelkaus, M. H. G. de Miranda, A. Pe’er, B. Neyenhuis, J. J. Zirbel, S. Kotochigova, P. S. Julienne, D. S. Jin and J. Ye, *A High Phase-Space-Density Gas of Polar Molecules*, Science, **322**, 231–235 (2008).
- [46] O. A. R. Board, *OpenMP*, <http://openmp.org/wp/openmp-specifications/>.
- [47] D. Abrahams, *Boost.Python library*, [http://www.boost.org/doc/libs/1\\_47\\_0/libs/python/doc/](http://www.boost.org/doc/libs/1_47_0/libs/python/doc/).
- [48] M. Frigo and S. G. Johnson, *The Design and Implementation of FFTW3*, Proceedings of the IEEE, **93**, 216–231 (2005), special issue on “Program Generation, Optimization, and Platform Adaptation”.



# Danksagung

Ich danke *Tilman Pfau* für die Betreuung und die ausführlichen wöchentlichen Diskussionen. Danke *Kazimierzowi Rządowskiemu* za bycie świetnym opiekunem i kilkukrotne zaproszenie mnie do Warszawy. Ich danke *Hans Peter Büchler* für die Übernahme des Mitberichts. Danke *Krzysztofowi Pawłowskiemu* za wiele dyskusji, za wspólne pisanie kodu symulacji, za świetną zabawę podczas wycieczek w Polsce i Niemczech, za wzięcie ze mną udziału w półmaratonie oraz za wszystkie wspólne biegi, rowerowe wycieczki i wspinaczki. Ich danke *Holger Kadau* für seine Geduld sich immer wieder meine neusten Resultate anzuhören (obwohl die „absolut sinnlos sind“). Ich danke *Stefan Müller* für sein fortwährend großes Interesse und die vielen Diskussionen. Je remercie *Juliette Billy* pour ses explications détaillées et son expérience. Muito obrigado ao Emanuel Henn por sua experiência e suas explicações detalhadas. Ich danke dem restlichen 5. *Physikalischen Institut* für Freitagmorgen-Frühstücke, Talks und jede Menge andere Aktivitäten. Besonders *Jonas Metz* für seine Doktorarbeit, die mir oft weitergeholfen hat sowie *Harald Kübler* und *Paul Rehme*, die unseren „Rechenmeister“ am laufen halten. Ich danke meinen *Freunden*, meiner *Familie* und *Kerstin* für eine tolle Zeit.